Tellus (2003), 55B, 555–579
Printed in UK. All rights reserved

TELLUS
ISSN 0280–6509

TransCom 3 CO_2 inversion intercomparison: 1. Annual mean control results and sensitivity to transport and prior flux information

By KEVIN ROBERT GURNEY[1]*, RACHEL M. LAW[2], A. SCOTT DENNING[1], PETER J. RAYNER[2], DAVID BAKER[3], PHILIPPE BOUSQUET[4], LORI BRUHWILER[5], YU-HAN CHEN[6], PHILIPPE CIAIS[4], SONGMIAO FAN[7], INEZ Y. FUNG[8], MANUEL GLOOR[9], MARTIN HEIMANN[9], KAZ HIGUCHI[10], JASMIN JOHN[8], EVA KOWALCZYK[2], TAKASHI MAKI[11], SHAMIL MAKSYUTOV[12], PHILIPPE PEYLIN[4], MICHAEL PRATHER[13], BERNARD C. PAK[13], JORGE SARMIENTO[7], SHOICHI TAGUCHI[14], TARO TAKAHASHI[15] and CHIU-WAI YUEN[10], [1]*Department of Atmospheric Science, Colorado State University, Fort Collins, CO 80523, USA;* [2]*CSIRO Atmospheric Research, PMB 1, Aspendale, Victoria 3195, Australia;* [3]*National Center for Atmospheric Research (NCAR), Boulder, CO 80303, USA;* [4]*Laboratoire des Sciences du Climat et de l'Environment (LSCE), F-91198 Gif-sur-Yvette Cedex, France;* [5]*National Oceanic and Atmospheric Administration (NOAA), Climate Monitoring and Diagnostics Laboratory, 326 Broadway R/CG1, Boulder, CO 80303, USA;* [6]*Department of Earth, Atmospheric, and Planetary Science, Massachusetts Institute of Technology (MIT), Cambridge, MA 0214, USA;* [7]*AOS Program, Princeton University, Sayre Hall, Forrestal Campus PO Box CN710 Princeton, NJ 08544-0710, USA;* [8]*Center for Atmospheric Sciences, McCone Hall, University of California, Berkeley, CA 94720-4767, USA;* [9]*Max-Planck Institute fur Biogeochemie, D-07701 Jena, Germany;* [10]*Meteorological Service of Canada, Environment Canada, Toronto, Ontario M3H 5T4, Canada;* [11]*Quality Assurance Section, Atmospheric Environment Division, Observations Department, Japan Meteorological Agency, 1-3-4 Otemachi, Chiyoda-ku, Tokyo 100-8122 Japan;* [12]*Institute for Global Change Research, Frontier Research System for Global Change, Yokohama, 236-0001 Japan;* [13]*Earth System Science, University of California, Irvine, CA 92697-3100, USA;* [14]*National Institute of Advanced Industrial Science and Technology, 16-1 Onogawa Tsukuba, Ibaraki 305-8569, Japan;* [15]*Lamont-Doherty Earth Observatory of Columbia University, Palisades, NY, USA*

(Manuscript received 22 May 2002; in final form 27 November 2002)

ABSTRACT

Spatial and temporal variations of atmospheric CO_2 concentrations contain information about surface sources and sinks, which can be quantitatively interpreted through tracer transport inversion. Previous CO_2 inversion calculations obtained differing results due to different data, methods and transport models used. To isolate the sources of uncertainty, we have conducted a set of annual mean inversion experiments in which 17 different transport models or model variants were used to calculate regional carbon sources and sinks from the same data with a standardized method. Simulated transport is a significant source of uncertainty in these calculations, particularly in the response to prescribed "background" fluxes due to fossil fuel combustion, a balanced terrestrial biosphere, and air–sea gas exchange. Individual model-estimated fluxes are often a direct reflection of their response to these background fluxes. Models that generate strong surface maxima near background exchange locations tend to require larger uptake near those locations. Models with weak surface maxima tend to have less uptake in those same regions but may infer small sources downwind. In some cases, individual model flux estimates cannot be analyzed through simple relationships to background flux responses but are

*Corresponding author.
e-mail: keving@atmos.colostate.edu

likely due to local transport differences or particular responses at individual CO_2 observing locations. The response to the background biosphere exchange generates the greatest variation in the estimated fluxes, particularly over land in the Northern Hemisphere. More observational data in the tropical regions may help in both lowering the uncertain tropical land flux uncertainties and constraining the northern land estimates because of compensation between these two broad regions in the inversion. More optimistically, examination of the model-mean retrieved fluxes indicates a general insensitivity to the prior fluxes and the prior flux uncertainties. Less uptake in the Southern Ocean than implied by oceanographic observations, and an evenly distributed northern land sink, remain in spite of changes in this aspect of the inversion setup.

1. Introduction

A quantitative understanding of the sources and sinks of atmospheric CO_2 is of vital importance for reliably predicting future CO_2 levels. The estimation of CO_2 sources and sinks can be approached in a variety of ways (Schimel et al., 2001). One approach is to use atmospheric CO_2 measurements to infer CO_2 fluxes through tracer transport inversion. This approach adjusts a series of regionally explicit "trial" fluxes to best match observed CO_2 concentrations to those simulated by an atmospheric transport model. Early inversions used two-dimensional transport models to calculate the latitudinal distribution of fluxes (e.g. Tans et al., 1990; Enting and Mansbridge, 1989; Ciais et al., 1995). Recent inversions have used three-dimensional models to estimate the longitudinal distribution of fluxes (e.g. Enting et al., 1995; Fan et al., 1998; Bousquet et al., 1999a;b; Kaminski et al., 1999). Interannual variations in fluxes have also been estimated (e.g. Rayner et al., 1999; Law, 1999; Bousquet et al., 2000; Baker, 2001).

A general concern with inversions is the sensitivity of the results to the atmospheric transport model used. This sensitivity is difficult to assess because the results to date have employed only one or two transport models in a given study. A goal of the TransCom series of experiments has been to assess the influence of different transport algorithms on the CO_2 inversion problem. The initial phases of TransCom conducted forward simulations of fossil and biospheric emissions of CO_2 (TransCom 1) (Law et al., 1996) and of SF_6 (TransCom 2) (Denning et al., 1999) to characterize model behaviour. The fossil CO_2 experiment indicated differences in simulated surface interhemispheric concentration gradients among the models of up to a factor of two. However, with no 'fossil-CO_2' observations to compare against, it was not possible to determine which simulated transport, if any, was correct. The SF_6 experiment, with relatively well known sources and observations, was intended to evaluate atmospheric transport and to identify which processes led to different model behaviour. Most of the models were reasonably successful in reproducing the marine boundary-layer observations of SF_6, but tended to overestimate the SF_6 at continental locations near sources. Those models that underestimated marine boundary-layer values due to excessive vertical convective transport tended to give better continental concentrations than the models with less convective transport.

Model differences were also large for the annual mean response to seasonal biospheric CO_2 exchange. Almost all models simulated elevated CO_2 concentrations at the surface in the northern middle latitudes due to the covariance between seasonal exchange and seasonal transport, the so-called 'seasonal rectifier effect' (e.g., Keeling et al., 1989; Denning et al., 1995), but zonal mean surface concentrations varied over 3 ppm among the models.

While these experiments provided useful insights into model behaviour, they did not directly address the sensitivity of inversion results to transport. This is the role of the current TransCom experiment (TransCom 3); the aim is to assess the contribution of uncertainties in transport to the uncertainties in flux estimates for annual mean, seasonal cycle and interannual inversions. The experiment can also contribute to our understanding of other sensitivities in the inversion process (e.g. inversion set-up, observational data choices), since more reliable results are expected by examining the sensitivity with a range of transport models than with just one or two models.

The first results from TransCom 3 were presented by Gurney et al. (2002). They showed mean inversion results for a 'control' inversion in which annual mean fluxes were estimated using 1992–1996 data. Here we present results from that same control inversion but for individual models. We also present results from a number of sensitivity tests related to the specification of prior flux information. A companion paper (Law et al., 2003) presents sensitivity tests related to CO_2 data issues including network choice, time period, data

selection and data uncertainty. Seasonal and interannual inversions will be presented elsewhere.

2. Method

2.1. Inversion formalism

The control inversion uses a Bayesian synthesis method (Enting, 2002). The first step is to choose a set of flux patterns, or basis functions ($\vec{V}_i$), from which solutions will be constructed: $\vec{V} = \sum_i s_i \vec{V}_i$. The inversion procedure reduces to solving for the scaling factor, s_i. With a set of concentration observations $\vec{D}$ the linearity of transport can be used to yield

$$\vec{D} = \sum_i s_i \mathbf{T}(\vec{V}_i) \tag{1}$$

where **T** is the atmospheric transport. If we have predefined times and places for our concentration observations (obvious in a diagnostic or inverse study) then we can repeatedly run the transport model on each basis function and sample the output at the observation locations. The concentration field generated from each basis function is referred to as its corresponding response function. If we sample the response function at our chosen observation locations, and write the result as a column vector, we produce a matrix **M** for which we can easily show

$$\vec{D} = \mathbf{M}\vec{S} \tag{2}$$

The regional fluxes, $\vec{S}$, can now be solved for using conventional least-squares techniques. These techniques rely on minimizing the mismatch between modelled concentrations, $\mathbf{M}\vec{S}$, and observed concentrations, $\vec{D}$. Adding prior information about the fluxes acknowledges the under-determinacy of the system due to the limitation of few observations to constrain fluxes from all regions. It also allows those aspects of the flux distribution that are reasonably well known to be specified.

With the addition of prior information, the solution for $\vec{S}$ now involves minimizing the difference between modelled and observed concentrations and between predicted fluxes and their prior estimates. A cost function J can be defined as

$$J = \frac{1}{2}\Big[(\mathbf{M}\vec{S} - \vec{D})^T \mathbf{C}(\vec{D})^{-1}(\mathbf{M}\vec{S} - \vec{D}) + (\vec{S} - \vec{S}_0)^T \mathbf{C}(\vec{S}_0)^{-1}(\vec{S} - \vec{S}_0)\Big] \tag{3}$$

where $\mathbf{C}(\_)$ embodies confidence in the form of an error or uncertainty covariance. Since **C** appears inverted, quantities with large uncertainty confer less influence. Deviations from this prior estimate will penalize the cost function severely, and hence be restricted. Alternatively, fluxes that are poorly understood can be assigned large uncertainties and, hence, allowed to deviate significantly from the prior estimates.

The measurements are similarly weighted inversely by the degree to which the predicted concentrations are required by the inverse process to match the observations. This weighting term, $\mathbf{C}(\vec{D})$, has traditionally been called the "data uncertainty". The name is misleading, since the term must also account for the inability of models with imperfect transport and coarse spatial and temporal resolution to match point observations. Furthermore, the chosen flux shape or "footprint" assumed for the basis functions may not represent the distribution of the true source field, and hence may add to the inability of the predicted concentrations to match observations (Kaminski et al., 2001; Engelen et al., 2002). It would be inappropriate in the inversion to attempt to fit the data better than the sum of all of these errors, yet objectively quantifying this overall model–data mismatch remains difficult.

Following Tarantola (1987) we minimize eq. (3) to yield

$$\vec{S} = \vec{S}_0 + \mathbf{M}^{(-1)}(\vec{D} - \mathbf{M}\vec{S}_0) \tag{4}$$

where $\mathbf{M}^{(-1)}$, the generalized inverse of **M**, is given by

$$\mathbf{M}^{(-1)} = \Big[\mathbf{M}^T \mathbf{C}(\vec{D})^{-1}\mathbf{M} + \mathbf{C}(\vec{S}_0)^{-1}\Big]^{-1} \mathbf{M}^T \mathbf{C}(\vec{D})^{-1}. \tag{5}$$

An estimate of the uncertainty in the predicted fluxes can also be produced. This depends on the uncertainty in the prior fluxes, the data uncertainty and the response functions embodied in **M**. The relation is:

$$\mathbf{C}(\vec{S}) = \Big[\mathbf{C}(\vec{S}_0)^{-1} + \mathbf{M}^T \mathbf{C}(\vec{D})^{-1}\mathbf{M}\Big]^{-1}. \tag{6}$$

This always represents a reduction in uncertainty on the prior estimate, with the amount of reduction depending on the data uncertainty and how well the

available observing locations sample the chosen flux patterns.

The mean of the individual model flux uncertainties can be computed as:

$$\overline{\mathbf{C}(\vec{S})} = \sqrt{\sum_{n=1}^{N_{\text{models}}} [\mathbf{C}(\vec{S})]^2 \Big/ N_{\text{models}}} \tag{7}$$

where the individual model posterior uncertainty estimates are taken from the diagonal of the posterior covariance matrix. We designate this mean uncertainty the 'within-model' uncertainty. The spread of flux estimates across models is represented by the standard deviation,

$$\sigma(\vec{S}) = \sqrt{\sum_{n=1}^{N_{\text{models}}} [\mathbf{C}(\vec{S}) - \overline{\mathbf{C}(\vec{S})}]^2 \Big/ N_{\text{models}}} \tag{8}$$

and designated the 'between-model' uncertainty.

The minimum value of the cost function, $J_{\min}$, describes the degree to which the inversion calculation matches the data and prior source estimates simultaneously. This is usually expressed using the reduced χ^2,

$$\chi^2 = \frac{\mathbf{J}_{\min}}{\mathbf{N}_{\text{obs}}} = \frac{\sum_{n=1}^{\mathbf{N}_{\text{obs}}} \frac{(\mathbf{M}\vec{S}-\vec{D})^2}{\mathbf{C}(\vec{D})^2} + \sum_{r=1}^{R_{\text{regions}}} \frac{(\vec{S}-\vec{S}_0)^2}{\mathbf{C}(\vec{S}_0)^2}}{\mathbf{N}_{\text{obs}}}. \tag{9}$$

Statistical consistency requires χ^2 not to be significantly greater than unity, otherwise the posterior uncertainty is inconsistent with the quality of the fit to the data. This inconsistency suggests that too much confidence has been placed in the ability of the inversion to match the data, so $\mathbf{C}(\vec{D})$ is increased accordingly. This will consequently increase $\mathbf{C}(\vec{S})$.

2.2. *Experimental design*

2.2.1. Forward simulations. Forward simulations were performed with 16 transport models (or model variants) (Gurney et al., 2000), the results of which were used to perform annual mean inversions for sources and sinks (Gurney et al., 2002). A 17th model (CSIRO) recently submitted simulations. We have not included results from this model in the calculation of mean results, in order to maintain consistency with Gurney et al. (2002), but have included it in presentations of individual model results. Details of each transport model are given in Table 1. The models vary in resolution, advection scheme, driving winds and subgrid-scale parameterizations. They include every model used in recently published CO_2 inversions. TM2 is the only model that has been used in precisely the same configuration in all the TransCom experiments, while seven of the current models performed the TransCom 2 SF_6 experiment, though some of these have been modified since that experiment.

For the annual mean experiment presented here, four-year simulations were performed by each model for each of 26 required basis functions. The 26 basis functions comprised four "background" global fluxes and 22 regional fluxes. The model output was submitted as global monthly mean distributions and as four-hourly time series at 228 specified locations. Sampling of model output was intended to mimic the sampling protocol for observations: some stations were moved offshore away from coastlines in the direction of the "clean air sector" identified for flask sampling. Full details of the experimental protocol are presented in Gurney et al. (2000). The inversions were performed on the output from each model.

The four background fluxes consisted of two fossil fuel emission fields (1990 and 1995 distributions), an annually balanced, seasonal terrestrial biosphere exchange and air–sea gas exchange. These fluxes are included in the inversion with a very small prior uncertainty so that their magnitude is effectively fixed, and the 22 regional fluxes estimated by the inversion are deviations from these global fluxes. The 1990 annual mean fossil source ($1^\circ \times 1^\circ$) is from Andres et al. (1996) and totals 5.812 Gt C yr^{-1}. The 1995 annual mean fossil source ($1^\circ \times 1^\circ$) is derived from the data prepared by Brenkert (1998) and totals 6.173 Gt C yr^{-1}. The seasonal biospheric exchange ($1^\circ \times 1^\circ$) was derived from the Carnegie Ames Stanford Approach (CASA) model (Randerson et al., 1997), and has an annual total flux of zero at every grid cell. The oceanic exchange ($4^\circ \times 5^\circ$) was produced by Taro Takahashi and colleagues and represents monthly global oceanic exchange derived from measurements of $\Delta p(CO_2)$ (Takahashi et al., 1999). The annually integrated flux is -2.19 Gt C yr^{-1} (into the ocean). The background fossil fuel emission fluxes were prescribed without seasonality. The annually balanced terrestrial fluxes were purely seasonal, and the background ocean fluxes were prescribed with both seasonal variations and annual mean uptake.

The boundaries of the 22 regional basis functions are shown in Fig. 1. In the forward simulations, each

Table 1. *Participating model description and references*

Model	Modeler	Winds	H. Res.	# Levels	Advection	Subgrid	References
CSU[a]	Gurney & Denning	Online	72 lon. × 44 lat.	17 sigma	2nd order	Cum. mass flux (Arakawa & Schubert, 1974; Randall & Pan, 1993; Ding et al., 1998), var. prog. PBL (Suarez et al., 1983; Randall et al., 1992)	Denning et al. (1996)
UCB[f]	Fung & John	1 h GISS GCM II′	72 lon. × 46 lat.	9 sigma	Slopes (Russell & Lerner, 1981)	Penetrative mass flux	Hansen et al. (1997)
UCI (s, b)[b]	Prather, Pak, Lee, & Hannegan	GISS GCM II′	72 lon. × 46 lat.	9 sigma & 23 sigma	2nd order moments (Prather, 1986)	Penetrative mass flux w/updrafts, downdrafts and entrainment; diurnally varying PBL	Prather et al. (1987); Hansen et al. (1997); Koch and Rind (1998)
JMA	Maki	6 h JMA (1997)	144 lon. × 73 lat.	32 hybrid	Hor: semi-lag., Vert: box scheme	Vert diff. (Mellor–Yamada, level 2.0), Cumulus (simple diff.), PBL (fixed layer)	Taguchi (1996)
MATCH: CCM3	Bruhwiler	NCAR CCM3	128 lon. × 64 lat.	28 sigma	Spitfire	Corrective transport, subgrid diff., PBL w/stable mixing, cloud prediction	Rasch et al. (1997)
MATCH: NCEP	Chen	6 h NCEP (1990)	128 lon. × 64 lat.	28 sigma	Spitfire	Vert. diff. w/diagnosed PBL; penetrative conv. + local conv. correction (Hack, 1994)	Rasch et al. (1997)
MATCH: MACCM2	Law	6 h MACCM2	64 lon. × 64 lat.	24 hybrid	Semi-lagrangian	Hack convection (Hack, 1994); vert. diff. with PBL (Holtslag & Boville, 1993)	Rasch et al. (1997); Law & Rayner (1999)
NIES	Maksyutov	12 h ECMWF (1997)	144 lon. × 72 lat.	15 sigma	Semi-lagrangian	Vert. diff. in troposphere (Hack, 1993); penetrative mass flux (Tiedke, 1989); vert. diff. in PBL (Schubert et al., 1993)	Maksyutov & Inoue (2000)

Table 1. *(cont'd.)*

Model	Modeler	Winds	H. Res.	# Levels	Advection	Subgrid	References
NIRE CTM-96[c]	Taguchi	6 h ECMWF (1995)	144 lon. × 73 lat.	15 hybrid	Semi-lagrangian	Vert. diff. in PBL, reduced diffusion at tropopause	Taguchi (1996)
RPN-SEF	Yuen & Higuchi	Online	128 lon. × 64 lat.	27 sigma	Semi-lag. (Richie & Beaudoin, 1994)	Vertical diffusion; PBL based on turbulent KE (Benoit et al., 1997)	D'Andrea et al. (1998)
SKYHI[d,f]	Fan	Online	100 lon. × 60 lat.	40 hybrid	2nd order	Dry/moist convective adjustment for T, q; non-local parameterization for vert. mixing in PBL	Mahlman et al. (1994); Strahan & Mahlman (1994); Hamilton et al. (1995)
TM2[e]	Bousquet & Peylin	12 h ECMWF (1990)	48 lon. × 25 lat.	9 sigma	Slopes (Russell & Lerner, 1981)	Mass flux (Tiedke, 1989); stability dependent vertical diffusion (Louis, 1979)	Heimann (1995); Bousquet et al. (1999a)
TM3[f]	Heimann	6 h ECMWF (1990)	72 lon. × 45 lat.	19 hybrid	Slopes (Russell & Lerner, 1981)	Mass flux (Tiedke, 1989); stability dependent vert. diffusion (Louis, 1979, updated)	Heimann (1995)
GCTM[e]	Baker	6 h ZODIAC GCM	256 km^2	11 sigma	2nd/4th order	Vert. diffusion, Ri number-based vert. mixing in lowest 3 layers to represent PBL.	Mahlman & Moxim (1978); Levy et al. (1982)
CSIRO-CC[g]	Kowalczyk & McGregor	Online	208 km^2	18 sigma	Hor: semi-lag (McGregor, 1996); Vert: total var diminishing	Stability dep. Vert. diff. (Louis, 1979) + non-local scheme, mass flux conv. w/downdrafts.	McGregor & Dix (2001)

[a]Participated in TransCom 1 and TransCom 2 but model differed.
[b]UCI primary model uses 3-hourly GISS II' 9-layer GCM winds and is primarily tropospheric; UCIb is a boundary-layer variant with PBL height diagnosed from Ri number, super-resolved tracer gradients using second-order moments, and non-local closure on the subgrid (Hartke and Rind, 1997); UCIs uses 6-hourly GISS II' middle atmosphere GCM winds with a well resolved stratosphere (Koch and Rind, 1998).
[c]Earlier model version participated in TransCom 1, current model version in TransCom 2.
[d]A non-local parameterization for vertical mixing in the PBL was implemented after TransCom 2 and was used in TransCom 3.
[e]Participated in TransCom 1 and TransCom 2 with current model.
[f]Participated in TransCom 2.
[g]Model output fields were interpolated from model's conformal-cubic grid to regular (2° latitude, longitude) grid before submission.

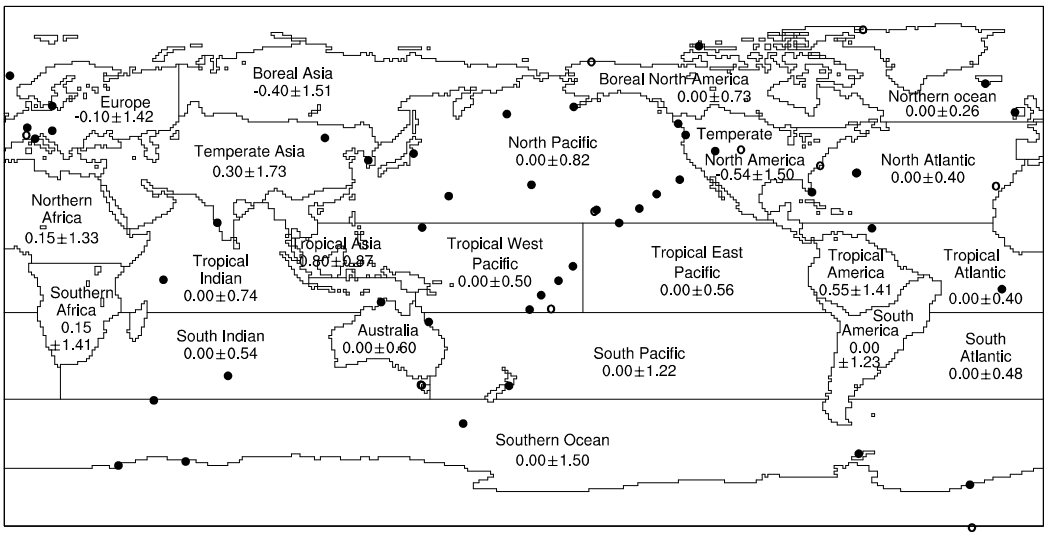

Fig. 1. Basis function regions and the locations of the 76 CO_2 observational records used in the inversion. Multiple records exist at some locations and are denoted by open circles. The prior flux and prior flux uncertainties are shown for each basis function region (Gt C yr^{-1}). The prior constraint on the atmospheric growth rate is 3.274 Gt C yr^{-1} with a prior uncertainty of 0.074 Gt C yr^{-1}. The prior global offset concentration is 355 ppm with a prior uncertainty of 100 ppm.

region emits a 1 Gt C yr^{-1} flux that is scaled independently during the inversion calculation. The regional terrestrial basis fluxes include spatial structure based on the distribution of annual mean net primary productivity (NPP), as given by a CASA model steady-state run (Randerson et al., 1997), reflecting an assumption that terrestrial exchanges are located within regions of higher biological activity. The terrestrial basis function boundaries were constructed to enclose vegetation of similar seasonal structure and carbon exchange, with some additional boundary smoothing. The starting point for the boundary construction was the $1^\circ \times 1^\circ$ land cover type classification used by the original Simple Biosphere Model (SiB) (De Fries and Townshend, 1994; Sellers et al., 1996). A uniform spatial distribution was used for the regional oceanic basis functions, with the exception of seasonal ice cover in the northern and southernmost regions. The sea-ice cover data were produced by the World Climate Research Programme, Working Group on Numerical Experimentation, Atmospheric Model Intercomparison Project (Taylor et al., 1997).

2.2.2. Inversion set-up and observational data. Prior estimates of the fluxes in each of the 22 regional basis functions were determined from independent estimates of terrestrial and oceanic exchange and are presented in Fig. 1. The land region prior flux estimates incorporate results from recent inventory studies (Apps and Kurz, 1994; Kurz and Apps, 1999; UNFCCC, 2000; Pacala et al., 2001; Houghton, 1999; Dixon et al., 1990; Houghton and Hackler, 1999; Kauppi et al., 1992). Where more than one estimate for a given region was available, a mid-point of the estimate range was used. The ocean region prior flux estimates were prescribed as zero.

The prior flux uncertainty is important for keeping the estimated fluxes within biogeochemically realistic bounds. For land regions we chose growing season net flux (GSNF, the sum of monthly mean exchange for months exhibiting net uptake) as provided by the CASA model of net ecosystem production (Randerson et al., 1997). Since it is unlikely that an annual mean residual land flux would exceed the GSNF, this provides a reasonable, ecologically relevant upper bound. The prior ocean uncertainties were guided by the aggregate estimates given in Takahashi et al. (1999), which suggest a total global oceanic uncertainty approximately 70% of the total oceanic exchange. Because this level of uncertainty tightly constrains some oceanic regions to the prior flux estimate, the aggregate uncertainty was increased to 140% of the total net oceanic exchange. The uncertainty in individual oceanic basis function regions was proportional to the

area of the region and the proportion of sampled grid points in the region.

We invert 5-yr mean measurements for 1992–1996 at 76 sites taken from the GLOBALVIEW-2000 dataset (GLOBALVIEW-CO_2, 2000). GLOBALVIEW is a data product that interpolates CO_2 measurements to a common time interval. Gaps in the data are filled by extrapolation from marine boundary-layer measurements. Sites were chosen where the extrapolated data accounts for less than 30% of total data for the 1992–1996 period. Law et al. (2003) varied this extrapolated data limit to test the sensitivity of the inversion to alternative data sets.

The uncertainty attached to each data value, *C(D)*, was derived from the residual standard deviation (RSD) of individual observations around a smoothed timeseries as given by GLOBALVIEW-CO_2 (2000). This choice was based on the assumption that the distribution of RSD (higher RSD values for northern and continental sites and lower RSD values for southern hemisphere oceanic sites) reflects the high-frequency variations in transport and regional flux that large-scale transport models are unable to accurately simulate. Direct use of the RSD values for the data uncertainty within the inversion results in a reduced χ^2 [eq. (9)] that is much smaller than unity. This indicates that the predicted concentrations fit the data much better than the uncertainty assigned to the data itself, and that the uncertainty should be reduced. Therefore, the RSD has been scaled as follows: the RSD was divided by $(8P)^{0.5}$, where P is the proportion of real data in the record and the factor 8 accomplishes the $\chi^2 \approx 1$ goal. Where this gave values less than 0.25 ppm, the uncertainty was increased to 0.25 ppm. Finally, the uncertainty was increased for those sites that are likely to occur in the same model grid cell by the square root of the number of co-located sites. This gave uncertainties ranging from 0.25 ppm for remote, "clean air" sites to 2.2 ppm for continental, "noisy" sites and a reduced χ^2 averaged across the models of 0.97, close to the desired value of one. Law et al. (2003) demonstrate the sensitivity of the inversion to the choice of C(D).

Additional prior constraints included in the inverse calculation are the global atmospheric CO_2 growth rate (3.274 ± 0.074 Gt C yr^{-1}) and a global CO_2 concentration background value (355 ± 100 ppm). The growth rate and uncertainty are the mean and standard deviation of the 1992–1996 trends at the observational stations used in this study via a fit that includes a linear trend and harmonics.

3. Results

3.1. Background simulation results

The forward simulations of the four background fluxes provide a measure of model-to-model transport differences, and explain many of the features found in the inferred regional fluxes to be discussed in Section 3.2. Figure 2 shows the surface CO_2 concentrations resulting from the sum of the background fluxes for each of the models. Maxima associated with the fossil fuel emissions and the annually balanced, seasonal biosphere exchange are evident and vary considerably from model to model. Maxima associated with the fossil fuel emissions are centered over the industrial source regions of the United States, Europe and the Asian Pacific. Maxima associated with rectification of the biosphere exchange are broadly distributed over forested areas in North America and Eurasia. Regional minima in concentration are simulated over the Southern Ocean and to a lesser extent over the North Atlantic Ocean in response to the background ocean fluxes. Surface concentration responses range from very weak (TM2 and the UCI variants) to strong but localized (GCTM) to very strong over large areas (MATCH:NCEP, UCB). As was found previously (Law et al., 1996; Denning et al., 1999), there does not appear to be a systematic difference between models driven by analyzed winds and those using GCM winds.

Figure 3 shows the zonal mean surface CO_2 concentration resulting from each of the background fluxes separately and summed. The maximum fossil fuel concentrations occur around 50 °N and vary by almost 2 ppm among the models. Southern Hemisphere concentrations also vary with CSU, MATCH:MACCM2 and NIRE producing the highest concentrations. The interhemispheric difference (IHD) (mean Northern Hemisphere surface-layer concentration minus mean Southern Hemisphere surface-layer concentration) in these simulated surface responses provides a convenient index (not always an accurate indicator; see Denning et al., 1999) to summarize both meridional and vertical model transport, and is indicated in the figure for the fossil fuel and total background responses. CSU, TM2 and JMA exhibit the smallest IHD values indicating relatively rapid mixing away from source areas (vertical or meridional or both). The ratio of largest fossil fuel IHD to smallest IHD is 1.5 compared to 2.0 for the fossil simulation results from TransCom 1, indicating a convergence of model simulations for this

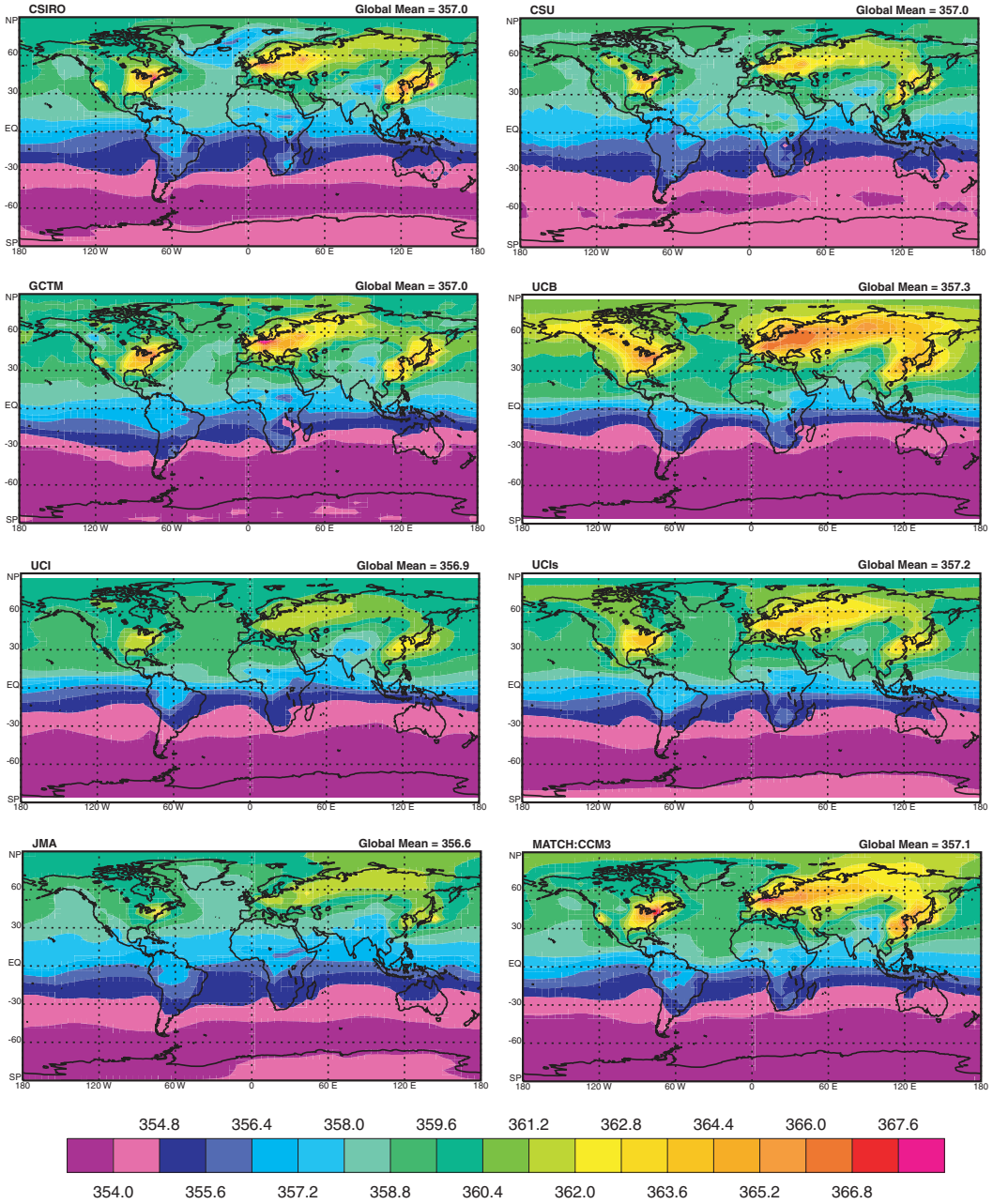

Fig. 2. Annual mean surface CO_2 concentration (ppm) resulting from the combined (relative to a background concentration of 350 ppm) background fluxes for each of the models. The UCIb model variant is not shown since its surface distribution is very similar to the UCI standard version. The global mean surface concentration is also computed for each model.

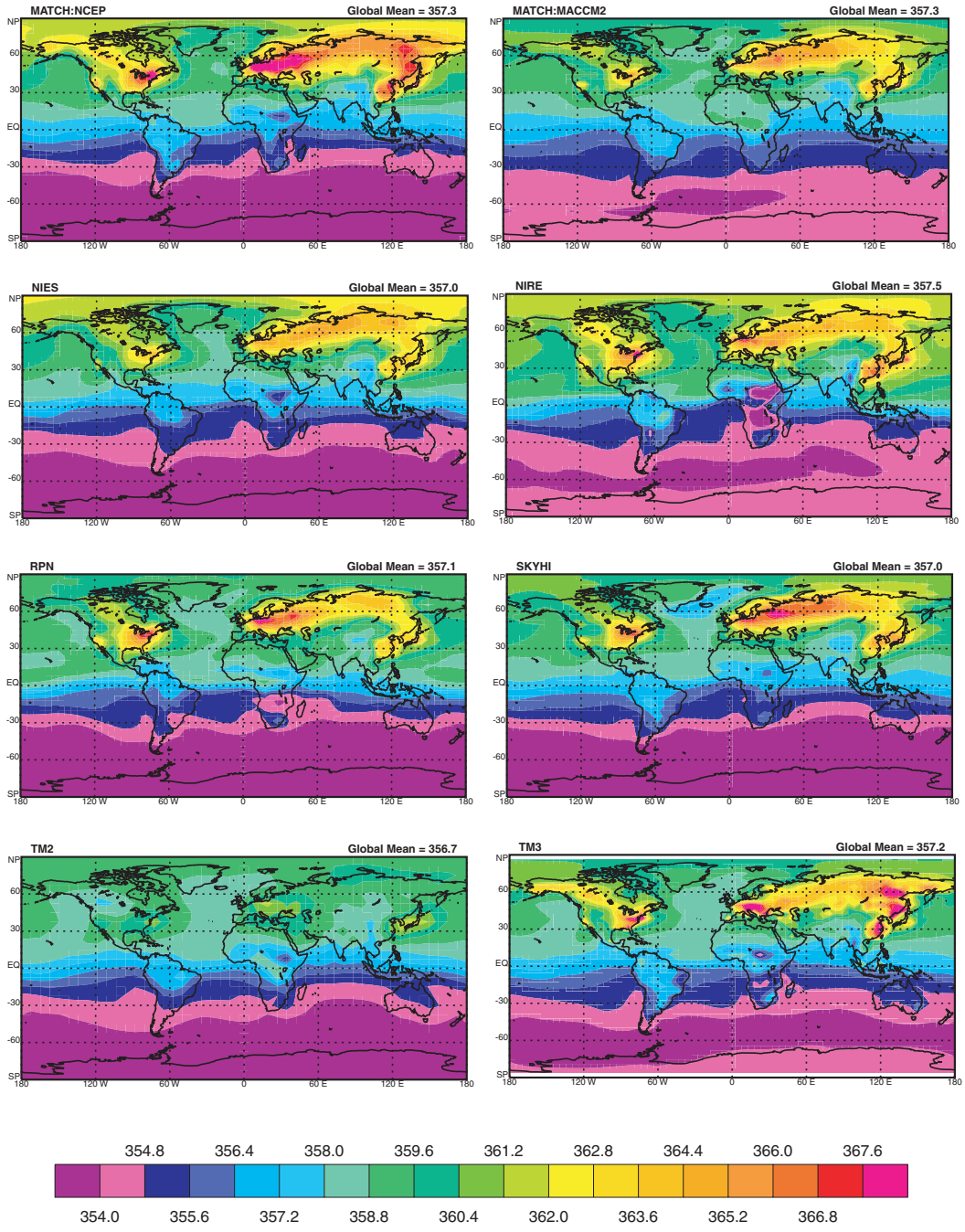
MATCH:NCEP
Global Mean = 357.3
MATCH:MACCM2
Global Mean = 357.3
NIES
Global Mean = 357.0
NIRE
Global Mean = 357.5
RPN
Global Mean = 357.1
SKYHI
Global Mean = 357.0
TM2
Global Mean = 356.7
TM3
Global Mean = 357.2
NP
60
30
EQ
-30
-60
SP
180
120 W
60 W
0
60 E
120 E
180
354.8
356.4
358.0
359.6
361.2
362.8
364.4
366.0
367.6
354.0
355.6
357.2
358.8
360.4
362.0
363.6
365.2
366.8

Fig. 2. (Contd.)

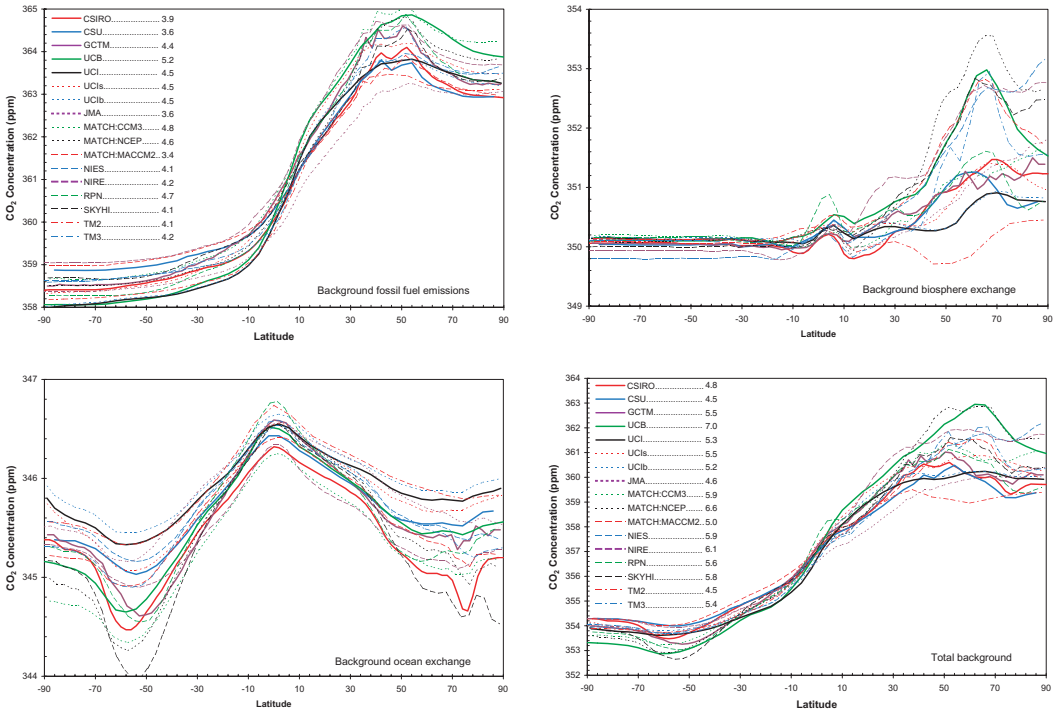

Fig. 3. Annual mean, zonal mean surface CO_2 concentration (ppm) resulting from the individual and combined (relative to a background concentration of 350 ppm) background fluxes for each of the models. The interhemispheric difference (ppm) for the background fossil and combined background CO_2 is listed in the key for each model. Note that the scale is different for each of the plots.

flux response. The 1990 fossil distribution used in this study is the same as that used in TransCom 1 but the total emission is 5.81 Gt C yr^{-1} compared to the 5.3 Gt C yr^{-1} previously used. Allowing for this difference, eight of the TransCom 1 models had IHDs below the current range (Law et al., 1996) indicating an evolution to less vigorous interhemispheric transport.

The zonal mean surface concentration for the biosphere exchange shows more spread in the northern mid- to high latitudes than for fossil fuel emissions. In TransCom 1 (using a different biosphere exchange) the model results clustered into two groups. Here, this clustering is less evident, with models spread throughout the 3.5 ppm range of concentrations around 60–70 °N. The highest concentrations (strongest rectification) are produced by MATCH:NCEP, while the weakest rectification is produced by the TM2 model. The RPN model produces relatively large equatorial concentrations, while the NIRE concentrations are greater than for other models around 20–30 °N. Besides the large variation in zonal mean response to these annually balanced fluxes, the models exhibit large variations in the spatial structure of the rectifier response within latitude zones (Fig. 2). Some strongly rectifying models (e.g., SKYHI, MATCH:MACCM2, RPN) limit concentration maxima to the immediate forcing areas over North America and Asia, where there are no stations. Others (NIES, NIRE, UCB, MATCH:NCEP) generate broad concentration maxima over the northern high latitudes and consequently have substantial impact at observing sites.

The zonal mean surface concentrations for the ocean exchange show similar structure for all models. The tropical source and extratropical uptake results in a small maximum concentration in the tropics, which varies by about 0.5 ppm across the models. Variations in the concentration minima are larger, particularly around 50–60 °S. SKYHI produces the lowest concentrations in both hemispheres, while MATCH:CCM3 exhibits low concentrations across all latitudes. RPN exhibits the largest equatorial maximum concentration. The greatest tropical/extratropical gradient is

exhibited by SKYHI, while UCI and UCIb exhibit the smallest gradients.

The zonal mean surface concentration for the total background fluxes shows how some models respond similarly to the background fluxes while others exhibit offsetting responses. For example, while responding strongly to fossil fuel fluxes over the northern extratropical source region, MATCH:CCM3 and RPN exhibit only a moderate response to the seasonal biosphere exchange. Similarly, MATCH:MACCM2 and NIES, which have a moderate fossil fuel response, show a stronger response to the seasonal biosphere exchange.

The remaining models show some similarity in their response to the background fluxes. In these cases, models that produce large surface gradients for fossil fuel also tend to produce large gradients for the background ocean exchange and exhibit a strong biospheric rectifier. This is broadly consistent with both vertical trapping of CO_2 in the lower model layers and with weaker advective mixing as compared to models exhibiting smaller gradients.

The spatial structure of surface CO_2 simulated by each model in response to the total of these background fluxes is different from the observed spatial variation of the observations. Because the background fluxes are fixed, the adjustment of the 22 regional fluxes is employed in the inversion to minimize this residual concentration response (RCR). The RCR values at all the observing stations (smoothed) is plotted for each model in Fig. 4. All models show positive RCR values in the northern mid-latitudes, implying the need for CO_2 uptake there. The greatest differences in RCR values between models are over the northern mid-latitudes (Fig. 4a). The standard deviation of these RCR values across the 17 models is less than 0.4 ppm at most stations, and greater than 1.0 ppm at 6 stations. The greatest variability is at Hungary ($\sigma = 2.4$ ppm; 47 °N, 16.7 °E).

Models with smaller background IHD values (CSU, JMA, MATCH:MACCM2) simulate higher RCR values over the southern extratropics relative to those with larger background IHD values (UCB, MATCH:NCEP, MATCH:CCM3). This suggests a potential relationship between interhemispheric transport and the magnitude of the inferred fluxes in the southern regions. Models with vigorous interhemispheric transport may require greater uptake over the southern extratropics relative to those models that exhibit weaker interhemispheric transport. Over the northern middle latitudes, where the model spread is greatest, the consistently largest RCR values are simulated by MATCH:NCEP, NIRE and UCB, and the smallest are simulated by TM2, CSU, CSIRO and JMA. These "clusters" of responses may produce similarly clustered inferred regional flux estimates.

The longitudinal distribution of the RCR values over the northern middle latitudes varied considerably among the models (Figs. 4b and 4c), particularly at continental sites near source regions (ITN, BAL, SCH and HUN). In general, RCR values increased from west to east across North America and Europe, which suggests the need for terrestrial uptake in these regions. The largest west to east gradients over North America were exhibited by NIRE and RPN, while the smallest belong to UCIb and TM2. UCIb and TM2 also had the smallest gradients over Europe while MATCH:NCEP and TM3 had the largest.

3.2. *Inversion results*

3.2.1. Model mean sensitivity. The model mean results for the control inversion were presented by Gurney et al. (2002). They found a Southern Ocean sink considerably weaker than the prior estimate of Takahashi et al. (1999). Furthermore, this result was not sensitive to the transport model used and was well constrained by observations. They also found reasonably strong data constraints over the northern continents, with uptake distributed relatively evenly across the northern land regions. Finally, they found a very weak data constraint in the tropics, with tropical flux estimates depending mostly on prior information, mass balance constraint and model transport.

To test the dependence of the model-mean inversion on the prior fluxes and their uncertainties, we performed the series of sensitivity tests described in Table 2. The first represents inversions in which the prior flux uncertainties for both land and ocean basis function regions were increased to 2, 5 and 10 Gt C yr^{-1}, bringing the inversions closer to methods that do not use prior information to constrain the flux estimates. The results of this test are presented in Fig. 5. For most regions, the mean flux estimates (X symbols) are very insensitive to the prior information, and lie within the uncertainty range of the control inversion. Exceptions are regions with few (or no) stations: the tropical and South Atlantic (all cases), northern Africa (± 5 and ± 10 Gt C yr^{-1} cases) and southern Africa and South America (± 10 Gt C yr^{-1} case).

For each model and region, the figure depicts an estimated flux and two uncertainty measures. The first

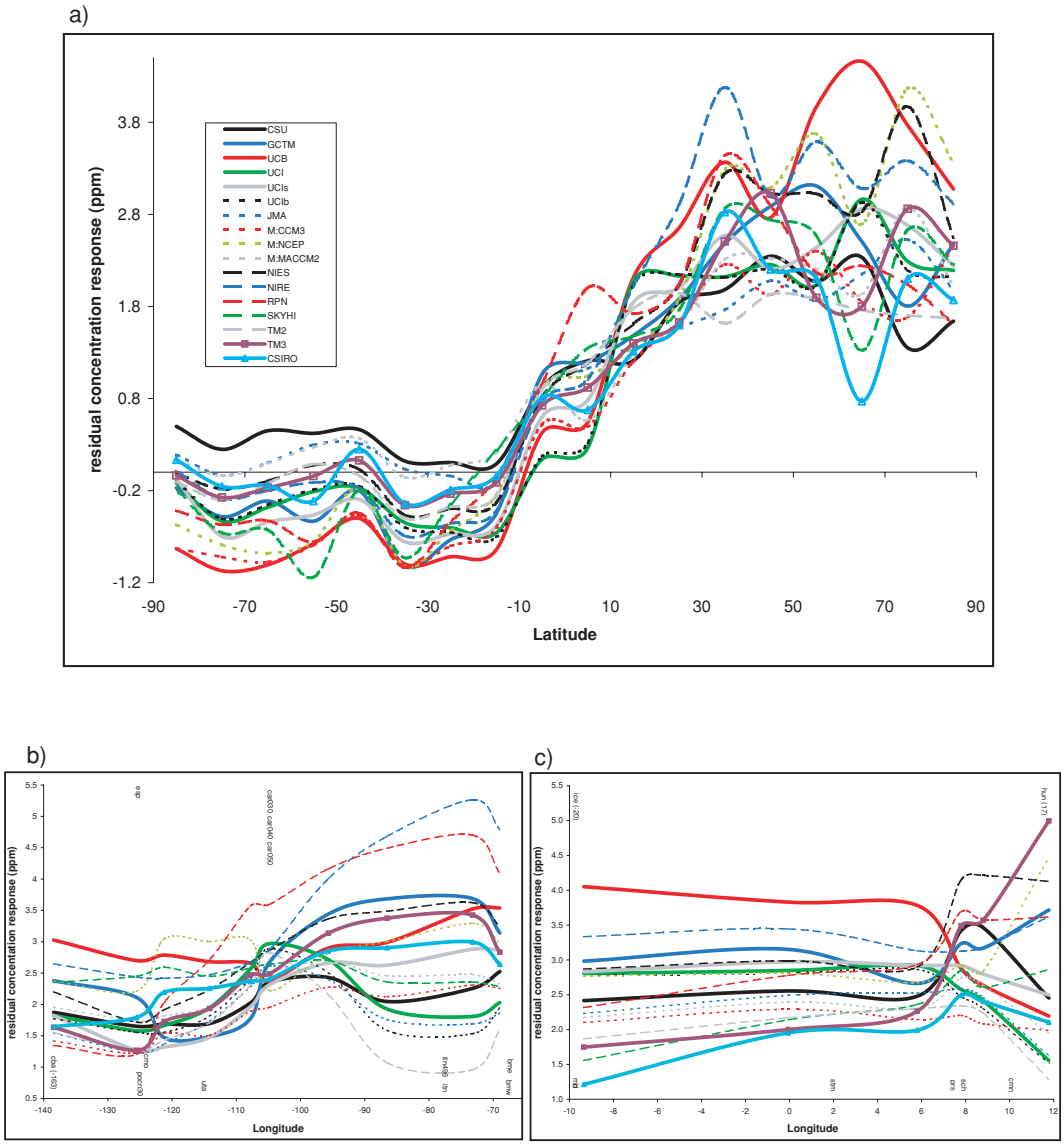

Fig. 4. (a) Smoothed (mean of 10° latitudinal bins) residual concentration response (ppm) at the 76 CO_2 observational stations for each of the models. (b) Smoothed (three station running mean) residual concentration response (ppm) at North American stations within the 30 °N to 70 °N longitudinal band. Longitudes are listed for stations located outside the center of the running mean. (c) Same as (b) but for Europe.

uncertainty measure is the within-model uncertainty (circles) defined in eq. (7). The magnitude of the decrease from the prior uncertainty indicates the degree to which the final flux estimate is constrained by the measurements. Figure 5 shows that for some regions the data constraint dominates. At the other extreme, the within-model uncertainty for some regions increases significantly as the prior flux uncertainty is increased. This indicates that these regions, for example tropical America, are poorly constrained by the CO_2 observations. Note that since the overall growth rate of CO_2 in the atmosphere is specified with small uncertainty

Table 2. *Brief description of the sensitivity tests*

Test 1 ("Loose Priors"): The prior flux uncertainties for both land and ocean basis function regions are increased to 2, 5 and 10 GtC yr^{-1}. These cases bring the inversion closer to those methods that do not use prior information to constrain the flux estimates.

Test 2 ("Zero Land Priors"): The prior basis function land fluxes are set to zero. Since many tropical regions are not well observed, it is important to check how sensitive the flux estimates are to the inclusion of land-use change information in the prior flux estimates.

Test 3 ("No Rect"): The background biospheric exchange is set to zero. This tests the sensitivity of the flux estimates to the rectifier. This case was also shown in Gurney et al. (2002) but here we also show individual model results.

Test 4 ("Adjust Rect"): The background biosphere exchange flux uncertainty is set to ±100%. This tests what rectifier magnitude the inversion estimates.

Test 5 ("Zero Ocean"): The background ocean exchange is set to zero. This tests whether the inversion is sensitive to the spatial distribution in the background ocean flux.

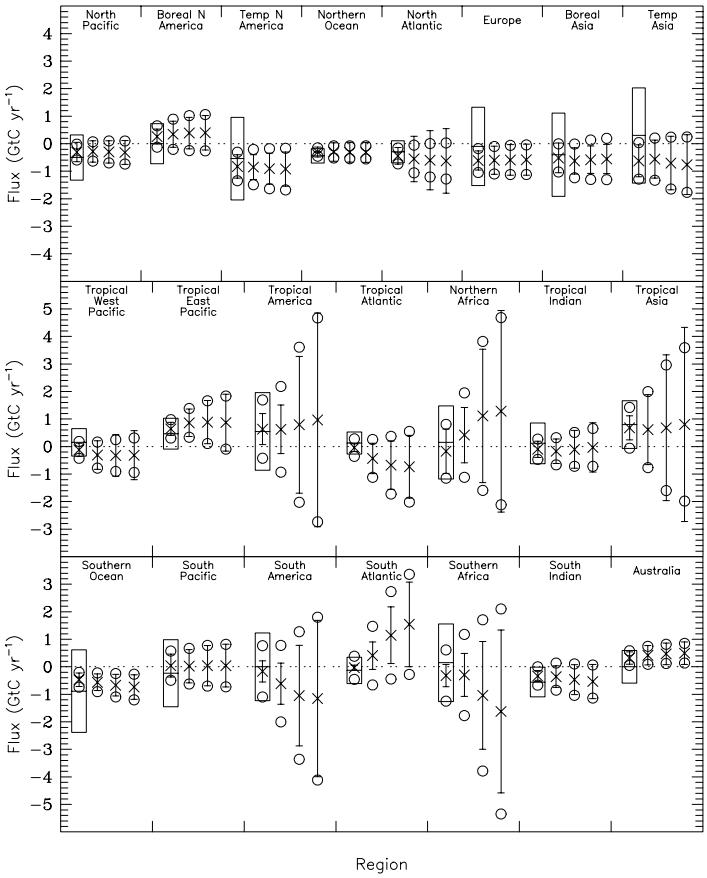

Fig. 5. Results of 'Loose Priors' case (sensitivity test 1). The control inversion is denoted by the leftmost set of symbols [crosses, posterior flux estimate (includes background ocean exchange); circles, within-model flux uncertainty; whiskers, between-model flux uncertainty; outer box, prior flux uncertainty]. The ±2 Gt, ±5 and ±10 Gt C yr^{-1} prior uncertainty cases are denoted progressively to the right of the control inversion. All uncertainties represent 1σ. Mean does not include CSIRO.

(0.074 Gt C yr^{-1}), the sum of the fluxes from the poorly constrained regions is fixed. As the priors are relaxed, dipoles of unrealistically large sources and sinks appear in these regions, but cancel each other to retain the observed mass of CO_2 in the atmosphere.

The second uncertainty measure is the standard deviation of the flux estimates across the ensemble of models (error bars) as defined in eq. (8). This measure indicates the degree to which transport model differences contribute to the range of flux estimates. Overall, the between-model uncertainty increases with the within-model uncertainty in Fig. 5. This reflects the increasing sensitivity of the inversion to differences in transport as the prior flux uncertainty is increased. As the priors are "loosened," we also obtain a somewhat closer fit to the observations: the mean data mismatch drops from 0.89 ppm for the control inversion to 0.77 ppm for ± 10 Gt C yr^{-1} case. This modest decrease in the mean data mismatch further suggests a general lack of sensitivity to the prior flux constraints chosen for the control inversion. The large between-model uncertainty in some regions means that, while the mean estimated flux can be relatively stable, individual models can give some very large fluxes. Overall, we conclude that in regions with strong data constraint, the inferred fluxes are insensitive to the prior fluxes, whereas in regions with few observations the fluxes are sensitive to both prior information and differences in model transport.

Figure 6 shows results from the other four sensitivity tests. When the land prior fluxes are set to zero only the estimated tropical Asian flux changes by greater

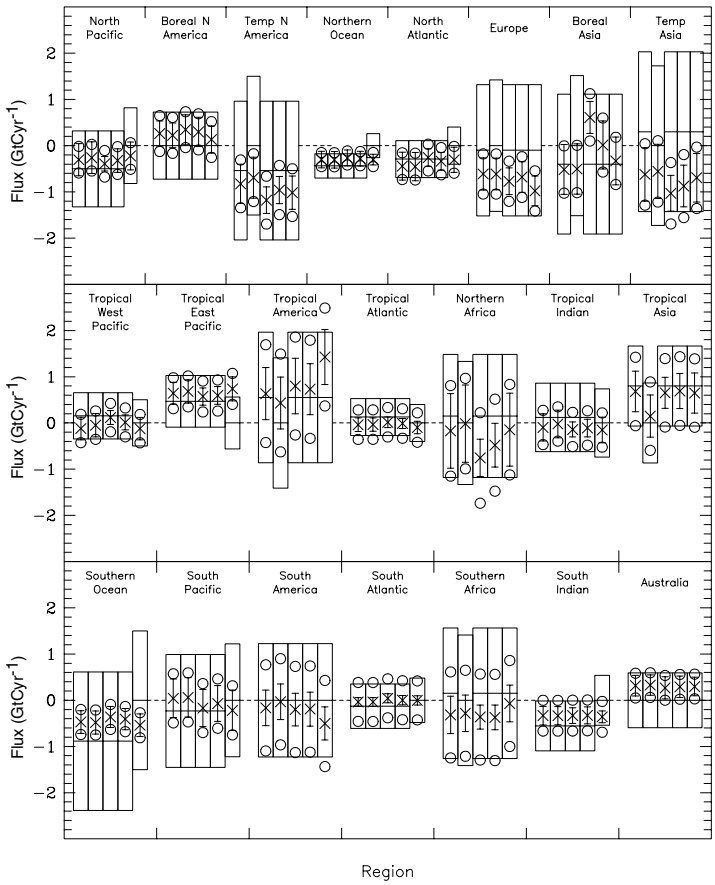

Fig. 6. Results of sensitivity tests 2–5. The control inversion is denoted by the leftmost set of symbols (as in Fig. 5). The 'Zero Land Priors' case (sensitivity test 2), 'No Rect' case (sensitivity test 3), 'Adjust Rect' case (sensitivity test 4), and 'Zero Ocean' (sensitivity test 5) are denoted progressively to the right. Mean does not include CSIRO.

than 0.2 Gt C yr^{-1}. Even for this region, the new flux estimate does not lie outside the control uncertainty range, which at 0.74 Gt C yr^{-1} is not much smaller than its prior uncertainty of 0.87 Gt C yr^{-1}. This is because none of the 76 sites used in the control inversion contributes much constraint to this region.

As described in Gurney et al. (2002), removing the background biosphere fluxes (third set of estimates in Fig. 6) has a large impact in some northern regions where rectification is pronounced; mean flux estimates change by up to 1.1 Gt C yr^{-1} and between-model uncertainty is generally reduced. For example, in almost all models, Boreal Asia changes from a moderate sink to a moderate source. In Test 4, we allow the inversion to optimize the magnitude of the seasonal rectifier by associating a large prior uncertainty ($\pm$100%) with the annually balanced biospheric flux. This tends to produce fluxes that are mid-way between the control and the 'No Rect' case, consistent with the 50% reduction in the model mean annually balanced biospheric exchange. In the final test, removing the background ocean flux had a larger impact in many of the land regions compared to oceanic regions, probably due to the generally larger prior uncertainties for land regions. However, none of the flux changes is larger than the control within-model uncertainties for the appropriate region.

3.2.2. Individual model results. Table 3 lists the control inversion flux estimates for the individual models when the land and ocean regions have been aggregated separately into the southern extratropics, tropics and northern extratropics. Figure 7 shows similar information, plotted as *differences from the model mean flux* for each region, along with flux differences for the 'No Rect' (test 3) and 'Zero Ocean' (test 5) sensitivity tests. The total land and total ocean flux estimates exhibit considerable spread and are anti-correlated since the total source is constrained. MATCH:NCEP and CSIRO produce flux estimates that lie outside the relatively large within-model uncertainties on the total land and total ocean regions. Removal of the background ocean flux reduces the extent to which these two models are outliers, with their flux estimates now inside the within-model uncertainty range. It is not clear why these two models respond in this way, since the strength of their responses to the background ocean tracer are similar to those of other models.

For the northern, tropical and southern regions, there is greater model spread for the aggregated land regions than for the oceans. This is driven by a combination of the larger variability in model response to annually balanced biospheric versus oceanic background fluxes (Figs. 2 and 3) and the larger prior flux uncertainties for land versus ocean regions. The influence of the annually balanced biospheric flux response is indicated by the considerable reduction in model spread in the 'No Rect' sensitivity test. Further evidence for this relationship is indicated by a strong correlation ($r = -0.74$) between the estimated northern land flux for each model and the annually balanced biosphere IHD values whereas there is no correlation with the fossil fuel IHD values ($r = -0.04$). Finally, the largest northern land changes between the control inversion and the 'No Rect' sensitivity test occur for those models with the largest rectifier: MATCH:NCEP, MATCH:MACCM2, NIES, UCB and TM3.

The tropical land flux estimates are negatively correlated ($r = -0.81$) with the northern land estimates. This occurs because the global growth rate is specified and with little observational constraint near the tropical continents, these tropical regions act as a repository for the flux residual remaining after optimization is made to regions with stronger observational constraints. Not surprisingly, MATCH:NCEP, with the largest rectifier, exhibits the largest tropical land flux change (2.2 Gt C yr^{-1} source to -0.1 Gt C yr^{-1} sink) when the rectifier is excluded in the 'No Rect' test.

The aggregated southern ocean flux estimates show the least amount of model spread. As suggested by the correlation ($r = 0.55$) between the total background flux IHD and the aggregated southern ocean posterior flux estimate, weaker interhemispheric transport (large background IHD values) correlates with less aggregated southern ocean uptake relative to the background ocean flux (-1.8 Gt C yr^{-1}). This lends support to our speculation that weak interhemispheric transport leads to lower southern hemisphere RCR values which, in turn, result in less uptake in the aggregated southern ocean relative to the background flux in this region. However, this relationship does not hold when the southern land and southern ocean are combined, suggesting the influence of other factors such as anomalously strong responses at particular stations or compensating tradeoffs with other regions.

Table 4 lists the individual model flux estimates and their uncertainties for all 22 land and ocean regions. Figure 8 shows similar information plotted as differences from the model mean flux for each region, for the control inversion and the 'No Rect' sensitivity test. Table 5 lists the change in individual model flux estimates when the inversion is run without the

Table 3. *Aggregated posterior fluxes and within-model uncertainties (1σ, $GtCyr^{-1}$) for individual models, control inversion*[a]

Model\Region	North land	North ocean	Tropical land	Tropical ocean	South land	South ocean	Total land	Total ocean
CSU	-2.5 ± 0.6	-1.7 ± 0.5	2.8 ± 1.4	0.9 ± 0.8	-0.7 ± 1.2	-1.6 ± 0.6	-0.5 ± 1.3	-2.4 ± 1.3
UCB	-2.9 ± 0.6	-1.1 ± 0.6	2.1 ± 1.3	0.3 ± 0.7	-0.4 ± 1.1	-0.8 ± 0.7	-1.1 ± 1.2	-1.7 ± 1.2
UCI	-1.4 ± 0.7	-1.6 ± 0.6	-0.3 ± 1.4	0.8 ± 0.7	0.7 ± 1.0	-1.0 ± 0.7	-1.1 ± 1.2	-1.7 ± 1.2
UCIs	-1.5 ± 0.7	-1.1 ± 0.6	-0.8 ± 1.3	1.1 ± 0.7	0.3 ± 1.2	-0.8 ± 0.7	$-2.0 \pm .13$	-0.8 ± 1.3
UCIb	-1.4 ± 0.7	-1.6 ± 0.6	-0.4 ± 1.4	0.9 ± 0.6	0.7 ± 1.0	-1.0 ± 0.7	-1.1 ± 1.1	-1.7 ± 1.1
JMA	-2.0 ± 0.7	-0.7 ± 0.6	0.9 ± 1.5	-0.0 ± 0.7	0.1 ± 1.2	-1.1 ± 0.8	-1.0 ± 1.3	-1.8 ± 1.3
M:CCM3	-2.5 ± 0.6	-0.7 ± 0.5	0.7 ± 1.3	0.6 ± 0.7	-0.3 ± 1.1	-0.6 ± 0.6	-2.1 ± 1.2	-0.7 ± 1.2
M:NCEP	-3.6 ± 0.5	-0.0 ± 0.4	2.2 ± 1.2	0.6 ± 0.7	-2.0 ± 1.0	0.1 ± 0.6	-3.4 ± 1.1	0.6 ± 1.1
M:MACCM2	-3.4 ± 0.6	-0.3 ± 0.5	1.8 ± 1.4	0.8 ± 0.8	-0.3 ± 1.2	-1.4 ± 0.7	-1.9 ± 1.2	-0.9 ± 1.2
NIES	-3.2 ± 0.6	-0.5 ± 0.4	2.2 ± 1.3	-0.3 ± 0.6	-0.1 ± 1.1	-0.8 ± 0.7	-1.2 ± 1.0	-1.6 ± 1.0
NIRE	-2.5 ± 0.6	-2.1 ± 0.4	1.2 ± 1.3	0.5 ± 0.5	0.4 ± 1.1	-0.4 ± 0.6	-0.8 ± 0.9	-2.0 ± 0.9
RPN	-2.0 ± 0.6	-1.3 ± 0.4	1.0 ± 1.0	-0.4 ± 0.7	-0.2 ± 0.9	0.1 ± 0.6	-1.2 ± 1.1	-1.6 ± 1.1
SKYHI	-3.2 ± 0.6	-0.9 ± 0.3	2.9 ± 1.3	-0.2 ± 0.6	-0.5 ± 1.1	-1.0 ± 0.6	-0.7 ± 1.0	-2.1 ± 1.0
TM2	-0.8 ± 0.6	-1.6 ± 0.5	-0.2 ± 1.5	-0.0 ± 0.5	0.6 ± 1.2	-0.9 ± 0.7	-0.3 ± 1.2	-2.5 ± 1.2
TM3	-3.1 ± 0.5	0.1 ± 0.4	1.4 ± 1.2	0.5 ± 0.6	-0.5 ± 1.1	-1.2 ± 0.7	-2.2 ± 1.1	-0.6 ± 1.1
GCTM	-1.2 ± 0.5	-1.6 ± 0.4	0.8 ± 1.4	0.2 ± 0.6	-0.4 ± 1.2	-0.5 ± 0.6	-0.9 ± 1.0	-1.9 ± 1.0
CSIRO	-2.7 ± 0.6	-0.1 ± 0.4	1.3 ± 1.3	0.5 ± 0.8	-1.3 ± 1.1	-0.5 ± 0.7	-2.7 ± 1.2	-0.1 ± 1.2
Mean	$\mathbf{-2.3 \pm 0.6}$	$\mathbf{-1.1 \pm 0.5}$	$\mathbf{1.1 \pm 1.3}$	$\mathbf{0.4 \pm 0.7}$	$\mathbf{-0.2 \pm 1.1}$	$\mathbf{-0.8 \pm 0.7}$	$\mathbf{-1.3 \pm 1.1}$	$\mathbf{-1.5 \pm 1.1}$

[a]The background ocean flux has been included in the oceanic fluxes. Regional aggregation is as follows: North land (Boreal North America, Temperate North America, Europe, Boreal Asia, Temperate Asia), North ocean (North Pacific, Northern Ocean, North Atlantic), Tropical land (Northern Africa, Tropical Asia, Tropical America), Tropical ocean (West Pacific, East Pacific, Tropical Atlantic, Tropical Indian), South land (Southern Africa, Australia, South America), South ocean (South Pacific, South Atlantic, South Indian, Southern Ocean). The mean sources do not include the CSIRO model. Units: GtC yr^{-1}

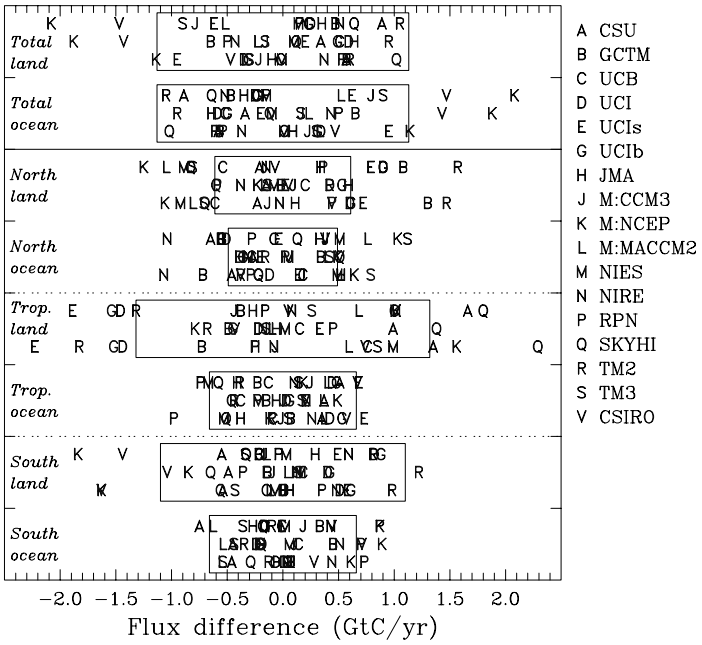

Fig. 7. Aggregated posterior flux differences from the model mean for the control inversion (top row in each box), the 'No Rect' case (sensitivity test 3, middle row in each box) and the 'Zero Ocean' case (sensitivity test 5, bottom row in each box). The box represents the within-model uncertainty (1σ). Regional aggregation is as follows: North land (Boreal N America, Temperate N America, Europe, Boreal Asia, Temperate Asia), North ocean (N Pacific, Northern Ocean, N Atlantic), Tropical land (Northern Africa, Tropical Asia, Tropical America), Tropical ocean (W Pacific, E Pacific, Tropical Atlantic, Tropical Indian), South land (Southern Africa, Australia, S America), South ocean (S Pacific, S Atlantic, S Indian, Southern Ocean).

background biospheric exchange. Most model flux estimates lie within the estimated uncertainty for the respective regions in Fig. 8. This demonstrates that the within-model uncertainty encompasses most transport differences with different models providing the extreme or outlying estimates in different regions. As was noted in the aggregated flux estimates, some of the outlying total zonal estimates can be attributed to the meridional gradient of the background fluxes. Results for the complete 22 basis function regions exhibits some longitudinal tradeoffs as well. For example, many models with large uptake in extratropical Asia such as MATCH:MACCM2. MATCH:NCEP and CSIRO show large downwind sources in the North Pacific region. Models with small combined uptake in extratropical Asia, such as TM2, show the largest uptake in the North Pacific.

The two models with the greatest combined uptake in North America, RPN (-1.11 Gt C yr^{-1}) and NIRE (-1.06 Gt C yr^{-1}), support the suggestion that large west to east declines in the RCR values are related to enhanced uptake. However, models with the smallest North American uptake (UCIb and GCTM) are not those with the smallest west to east gradient. Over Europe, the models with the smallest west to east gradient, UCIb and TM2, are among the three models with the smallest European uptake. Among those with the largest European west to east RCR gradient, both NIES and TM3 also exhibit among the greatest levels of uptake. UCB, however, has an average gradient but considerable uptake in Europe. In northern extratropical Asia, the relationship between the RCR west to east gradient and the estimated flux appears less consistent.

Another example of a relationship between the background fluxes and the model estimates of region-specific fluxes arises in the Southern Ocean region. Models that estimated the smallest uptake for the Southern Ocean region, SKYHI and MATCH:NCEP, were also models that responded most strongly to the background ocean flux (Figs. 2 and 3), particularly in the southern extratropics. They were also among the models with the lowest RCR values in the southern extratropics. Similarly, the responses of the CSIRO

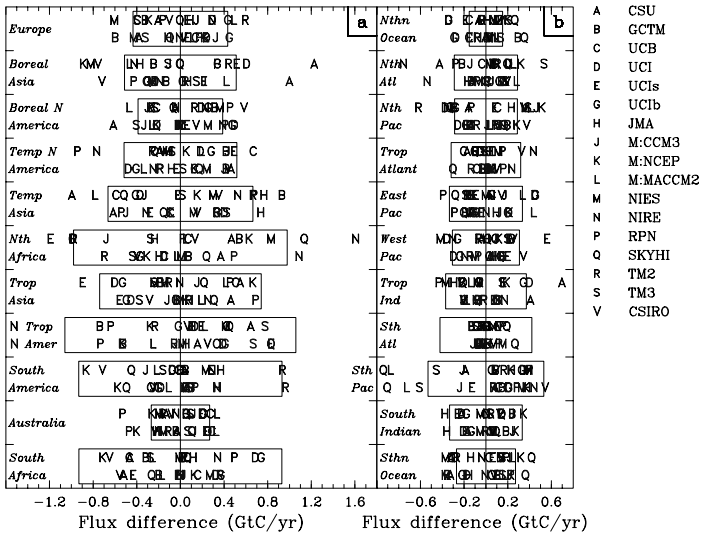

Fig. 8. Posterior flux differences from the 16 model mean for the control inversion (top row in each box) and the 'No Rect' case (sensitivity test 3, bottom row in each box). The boxes represent the 16 model mean within-model uncertainty (1σ).

and SKYHI models to the background ocean flux in the northern extratropics were the most pronounced (Fig. 3) and they also produced the least uptake in the northern ocean.

In contrast to the dependence of the estimated fluxes on the gradients in the background concentrations, there are a variety of instances in which outlying flux estimates are much more dependent on model responses at particular sites. For example, two models produce very large uptake for temperate North America, NIRE and RPN, but for different reasons. RPN is one of two models with a pronounced fossil fuel response, particularly over temperate North America. RPN also exhibits one of the weaker rectifier responses. As a result, RPN exhibits the largest uptake for the temperate North American region but shows little change in North America when the background biospheric exchange is removed. NIRE has larger responses than other models at Key Biscayne for background fossil and biospheric fluxes and for the temperate North American region. This results in significant uptake for the NIRE model in the temperate North American region, greater than all the models except RPN. This is confirmed by an inversion in which CO_2 data for Key Biscayne are excluded. The NIRE flux difference from the mean is reduced from -0.76 to -0.24 Gt C yr^{-1}.

As with the aggregated flux estimates, Table 5 shows significant changes over the northern land regions when the background biosphere exchange is removed from the inversion. In particular, large changes occur over Boreal Asia where nearly all of the models shift from uptake to emissions. The tropical land regions also exhibit shifts when inverting without the annually balanced biosphere. In particular, northern Africa becomes a sink instead of a source in many models (or in the case of NIRE, a much reduced source) when the annually balanced biosphere is removed. This apparent compensation between northern rectifier response and tropical terrestrial fluxes results from the global mass balance constraint and the relatively small ocean priors.

Models that exhibit significant surface gradients in response to the biospheric exchange are not always the models showing large shifts when the inversion excludes this background flux. This is due to the spatial pattern of the rectifier in relation to the position of the observational stations. For example, SKYHI shows one of the larger rectifiers (Figs. 2 and 3), but shows only a moderate shift in estimated flux when the background biospheric flux is removed. This is due to the somewhat limited horizontal transport of background biospheric flux near the surface over northern and eastern Asia. Since the four stations nearest to this region are located towards the eastern edge of the Asian continent, the response at these stations does not reflect the strength of the SKYHI rectification over central portions of Asia.

Table 4. *Posterior fluxes and uncertainties (1σ, $GtCyr^{-1}$) for individual models, control inversion*[a]

Region\Model	CSU	UCB	UCI	UCIs	UCIb	JMA	MATCH: CCM3	MATCH: NCEP
Boreal NA	0.21 ± 0.57	0.04 ± 0.23	0.45 ± 0.29	0.00 ± 0.37	0.51 ± 0.27	0.22 ± 0.53	−0.04 ± 0.04	−0.01 ± 0.38
Temperate NA	−1.02 ± 0.57	−0.16 ± 0.55	−0.64 ± 0.62	−0.34 ± 0.61	−0.55 ± 0.62	−0.93 ± 0.64	−0.40 ± 0.53	−0.77 ± 0.43
Trop America	1.28 ± 1.09	1.06 ± 1.06	0.76 ± 1.02	0.83 ± 1.04	0.61 ± 0.99	0.74 ± 1.13	0.72 ± 1.06	0.36 ± 1.09
South America	−0.13 ± 0.98	−0.18 ± 0.91	−0.24 ± 0.90	0.12 ± 0.96	−0.24 ± 0.90	0.20 ± 1.01	−0.48 ± 0.94	−1.03 ± 0.88
Northern Africa	0.30 ± 1.08	−0.10 ± 0.94	−1.16 ± 0.95	−1.36 ± 0.86	−1.16 ± 0.95	−0.41 ± 1.08	−0.85 ± 0.97	0.46 ± 0.91
Southern Africa	−0.78 ± 0.80	−0.79 ± 0.82	0.37 ± 0.64	−0.31 ± 1.02	0.42 ± 0.66	−0.20 ± 1.13	−0.29v0.78	−1.03 ± 0.74
Boreal Asia	0.71 ± 0.52	−0.53 ± 0.55	0.09 ± 0.58	0.00 ± 0.53	−0.18 ± 0.56	−0.89 ± 0.55	−0.63 ± 0.64	−1.41 ± 0.43
Temperate Asia	−1.62 ± 0.79	−1.21 ± 0.59	−0.99 ± 0.81	−0.64 ± 0.69	−1.03 ± 0.79	0.14 ± 0.79	−0.96 ± 0.60	−0.47 ± 0.54
Tropical Asia	1.23 ± 0.73	1.19 ± 0.79	0.08 ± 0.80	−0.22 ± 0.73	0.15 ± 0.80	0.54 ± 0.70	0.83 ± 0.78	1.34 ± 0.76
Australia	0.19 ± 0.33	0.59 ± 0.36	0.52 ± 0.34	0.51 ± 0.30	0.53 ± 0.29	0.12 ± 0.26	0.43 ± 0.30	0.05 ± 0.19
Europe	−0.82 ± 0.50	−1.01 ± 0.39	−0.32 ± 0.52	−0.55 ± 0.43	−0.18 ± 0.54	−0.52 ± 0.54	−0.47 ± 0.51	−0.90 ± 0.30
N Pacific	−0.46 ± 0.28	−0.20 ± 0.35	−0.68 ± 0.37	−0.22 ± 0.33	−0.58 ± 0.34	−0.07 ± 0.40	0.16 ± 0.31	0.21 ± 0.23
W Pacific	−0.16 ± 0.30	−0.04 ± 0.35	−0.48 ± 0.35	0.44 ± 0.31	−0.38 ± 0.29	−0.12 ± 0.37	−0.03 ± 0.32	0.00 ± 0.35
E Pacific	0.67 ± 0.45	0.70 ± 0.34	1.09 ± 0.33	0.55 ± 0.30	1.10 ± 0.33	0.49 ± 0.36	0.81 ± 0.39	0.53 ± 0.39
S Pacific	−0.15 ± 0.48	0.09 ± 0.59	0.38 ± 0.56	0.12 ± 0.63	0.37 ± 0.50	0.28 ± 0.61	−0.18 ± 0.52	0.27 ± 0.51
Northern Ocean	−0.37 ± 0.15	−0.46 ± 0.17	−0.65 ± 0.21	−0.49 ± 0.18	−0.64 ± 0.20	−0.29 ± 0.17	−0.24 ± 0.12	−0.10 ± 0.13
N Atlantic	−0.87 ± 0.35	−0.48 ± 0.29	−0.24 ± 0.32	−0.38 ± 0.32	−0.37 ± 0.29	−0.36 ± 0.33	−0.59 ± 0.30	−0.12 ± 0.28
Tropical Atlantic	−0.21 ± 0.31	−0.24 ± 0.34	−0.09 ± 0.36	0.02 ± 0.33	−0.09 ± 0.35	−0.01 ± 0.34	−0.01 ± 0.32	−0.04 ± 0.34
S Atlantic	−0.05 ± 0.44	−0.12 ± 0.44	−0.04 ± 0.46	0.08 ± 0.43	−0.03 ± 0.46	−0.03 ± 0.43	−0.10 ± 0.45	−0.05 ± 0.43
Southern Ocean	−0.79 ± 0.29	−0.44 ± 0.23	−0.75 ± 0.36	−0.41 ± 0.26	−0.79 ± 0.35	−0.61 ± 0.27	−0.25 ± 0.22	−0.15 ± 0.19
Trop Ind Ocean	0.60 ± 0.50	−0.17 ± 0.32	0.30 ± 0.40	0.06 ± 0.46	0.25 ± 0.33	−0.39 ± 0.43	−0.15 ± 0.38	0.09 ± 0.36
S Indian Ocean	−0.56 ± 0.37	−0.34 ± 0.36	−0.56 ± 0.41	−0.59 ± 0.39	−0.51 ± 0.39	−0.71 ± 0.38	−0.10 ± 0.33	0.01 ± 0.27
Glbl offset (ppm)	352.9 ± 0.2	352.6 ± 0.2	352.6 ± 0.2	352.3 ± 0.2	352.4 ± 0.2	352.9 ± 0.2	352.3 ± 0.2	352.5 ± 0.2

[a]The background ocean flux has been included in the oceanic fluxes.

Some ocean regions also show significant shifts between inversions with and without the biosphere exchange. For example, both the North Pacific and North Atlantic exhibit the largest ocean region shifts between the two cases, highlighting the downwind transport of the rectifier signal.

4. Discussion and conclusions

The TransCom 3 experiment has afforded the first thorough investigation of the extent to which transport differences among tracer models contribute to the overall uncertainty in inversion estimates of carbon sources and sinks. Fortunately, most of the models that have been used to perform carbon cycle inversions in the last decade participated in the current experiment. In addition to investigating the sensitivity of carbon inversions to transport, we have been able to compute a model mean result and test the sensitivity of the model mean to various aspects of the inversion setup. A companion paper (Law et al., 2003) extends these sensitivity tests by exploring the response of the model mean and individual model flux estimates to changes in the observation network, the observational uncertainties, baseline data selection criteria and time period.

The first and perhaps most important result of this experiment is that model transport is as large a contributor to the inversion uncertainty as the error produced by limited CO_2 observations. Some of the individual model estimated fluxes can be readily attributed to how they respond to the background flux fields. Models that exhibited large CO_2 concentration maxima near and downwind of large background fluxes estimate large uptake in those same regions in order to best match the CO_2 observations. Models with small CO_2 concentration maxima estimated less uptake near the background fluxes but compensated further downwind over ocean regions with weaker sources or small sinks. The model response to background fluxes was not always the best predictor, however. Many of the regional flux estimates for individual models were the result of strong responses at particular stations or subtle tradeoffs and compensation among regions.

The response to surface SF_6 fluxes was evaluated in the previous TransCom 2 experiment (Denning et al., 1999). Models exhibiting small surface concentration maxima like TM2 and an earlier variant of the UCB model systematically underestimated the observed meridional gradient of SF_6 in the remote marine boundary layer, so these models probably also underestimate regional fluxes in the present inversions. On the other hand, models exhibiting large surface

Table 4. *(cont'd.)*

MATCH: MACCM2	NIES	NIRE	RPN	SKYHI	TM2	TM3	GCTM	CSIRO
−0.21 ± 0.32	0.62 ± 0.44	0.49 ± 0.44	0.71 ± 0.28	0.20 ± 0.37	0.39 ± 0.51	0.03 ± 0.52	0.57 ± 0.25	0.33 ± 0.41
−0.64 ± 0.50	−0.95 ± 0.46	−1.60 ± 0.44	−1.77 ± 0.33	−1.06 ± 0.49	−1.09 ± 0.47	−0.91 ± 0.41	−0.41 ± 0.51	−0.63 ± 0.48
0.85 ± 1014	1.05 ± 10.2	−0.89 ± 1.07	−0.01 ± 0.95	1.08 ± 0.98	0.40 ± 1.18	1.41 ± 0.92	−0.11 ± 1.17	0.87 ± 1.05
−0.39 ± 1.00	0.07 ± 0.94	0.12 ± 0.91	−0.17 ± 0.85	−0.62 ± 0.85	0.77 ± 0.99	−0.33 ± 0.92	−0.12 ± 0.95	−0.85 ± 0.87
−0.12 ± 1.13	0.66 ± 0.88	1.44 ± 0.94	−0.15 ± 0.80	0.96 ± 1.06	−1.15 ± 1.08	−0.45 ± 0.95	0.37 ± 1.02	−0.05 ± 1.01
−0.58 ± 1.15	−0.33 ± 0.91	0.02 ± 0.93	0.18 ± 0.51	−0.25 ± 1.19	−0.28 ± 1.02	−0.59 ± 1.04	−0.64 ± 1.17	−0.81 ± 1.15
−0.99 ± 0.63	−1.34 ± 0.37	−0.94 ± 0.44	−0.18 ± 0.48	−0.52 ± 0.40	−0.08 ± 0.54	−0.63 ± 0.48	−0.76 ± 0.38	−1.70 ± 0.58
−1.41 ± 0.71	−0.32 ± 0.62	−0.10 ± 0.68	0.05 ± 0.67	−1.14 ± 0.62	0.04 ± 0.61	−0.61 ± 0.36	0.31 ± 0.59	−0.24 ± 0.70
1.09 ± 0.79	0.44 ± 0.72	0.67 ± 0.67	1.13 ± 0.66	0.90 ± 0.68	0.57 ± 0.79	0.44 ± 0.72	0.49 ± 0.72	0.44 ± 0.72
0.65 ± 0.35	0.12 ± 0.24	0.27 ± 0.15	−0.22 ± 0.22	0.37 ± 0.22	0.15 ± 0.14	0.41 ± 0.27	0.36 ± 0.19	0.40 ± 0.36
−0.13 ± 0.51	−1.22 ± 0.35	−0.32 ± 0.29	−0.78 ± 0.34	−0.62 ± 0.33	−0.02 ± 0.58	−1.01 ± 0.29	−0.94 ± 0.32	−0.47 ± 0.41
0.10 ± 0.33	0.06 ± 0.21	−0.66 ± 0.21	−0.44 ± 0.18	−0.63 ± 0.16	−0.92 ± 0.30	0.08 ± 0.26	−0.60 ± 0.21	0.28 ± 0.26
0.09 ± 0.38	−0.54 ± 0.30	−0.43 ± 0.21	−0.18 ± 0.18	−0.10 ± 0.34	−0.19 ± 0.28	0.08 ± 0.26	0.11 ± 0.26	−0.11 ± 0.36
0.98 ± 0.33	0.64 ± 0.33	0.69 ± 0.27	0.25 ± 0.32	0.36 ± 0.34	0.47 ± 0.20	0.46 ± 0.32	0.51 ± 0.28	0.76 ± 0.42
−0.84 ± 0.56	0.42 ± 0.43	0.44 ± 0.28	0.44 ± 0.43	−0.90 ± 0.52	0.20 ± 0.52	−0.41 ± 0.66	0.13 ± 0.57	0.02 ± 0.60
−0.19 ± 0.13	−0.19 ± 0.17	−0.23 ± 0.14	−0.17 ± 0.13	−0.04 ± 0.09	−0.34 ± 0.18	−0.09 ± 0.13	−0.34 ± 0.09	0.09 ± 0.08
−0.20 ± 0.30	−0.41 ± 0.29	−1.20 ± 0.26	−0.72 ± 0.26	−0.25 ± 0.20	−0.34 ± 0.27	0.09 ± 0.27	−0.67 ± 0.27	−0.51 ± 0.28
−0.04 ± 0.31	0.08 ± 0.34	0.40 ± 0.28	0.11 ± 0.29	−0.14 ± 0.28	−0.13 ± 0.32	−0.06 ± 0.32	−0.14 ± 0.24	0.33 ± 0.32
−0.17 ± 0.42	0.02 ± 0.37	0.03 ± 0.39	0.12 ± 0.43	0.15 ± 0.33	−0.08 ± 0.43	−0.13 ± 0.41	−0.17 ± 0.41	0.19 ± 0.37
−0.24 ± 0.27	−0.84 ± 0.30	−0.51 ± 0.29	−0.29 ± 0.24	−0.05 ± 0.16	−0.74 ± 0.35	−0.32 ± 0.25	−0.34 ± 0.22	−0.34 ± 0.16
−0.24 ± 0.44	−0.47 ± 0.34	−0.18 ± 0.26	−0.53 ± 0.39	−0.31 ± 0.31	−0.15 ± 0.25	0.05 ± 0.33	−0.32 ± 0.29	−0.44 ± 0.43
−0.19 ± 0.27	−0.38 ± 0.31	−0.33 ± 0.31	−0.20 ± 0.33	−0.19 ± 0.26	−0.29 ± 0.34	−0.29 ± 0.29	−0.09 ± 0.26	−0.34 ± 0.33
352.6 ± 0.2	352.7 ± 0.2	352.3 ± 0.2	352.5 ± 0.2	352.6 ± 0.2	352.7 ± 0.2	352.6 ± 0.2	352.5 ± 0.2	352.6 ± 0.2

concentration maxima like TM3, which performed better at marine stations, tended to overestimate continental concentrations of SF_6 near source regions, possibly reflecting excessive vertical trapping of tracer. A combination of model resolution, resolved advective transport and subgrid-scale vertical transport defines this tradeoff between meridional gradients and regional concentration extrema which produce most of the variability in model response and therefore in flux uncertainty.

When the fluxes in the current experiment are aggregated into three zonal bands for the ocean and land, they provide some instructive examples of model behaviour in estimating zonally integrated fluxes. The tight ocean constraints of the inversion setup and the greater variability in model response to the terrestrial background fluxes explain the greater model spread in the estimates for land versus ocean regions. Removal of the background biospheric exchange considerably reduces the model spread over land. Furthermore, the tropical land exchange is inversely related to the northern land uptake, highlighting the influence of the limited observational constraint in the tropical regions and the required compliance with the overall meridional gradient in the CO_2 observations. The influence of the rectifier emphasizes the need to observe and understand this phenomenon. Because incorrect spatial and temporal structure in this background flux cannot be adjusted by the inversion procedure, errors in the specification of the background flux will be aliased into errors in the regional flux estimates. Future TransCom work in which fluxes are adjusted on a monthly basis will eliminate much of the fixed temporal structure required by the current annual mean inversion.

The last conclusion that can be drawn from the aggregated flux estimates is the relationship between the Southern Ocean uptake and interhemispheric transport; models with large background flux IHDs and hence weak interhemispheric transport tend to estimate the greatest reduction in uptake when compared to the background ocean flux for this region. Like many of the other broad relationships between the background fluxes and the estimated model fluxes, this relationship is not universal to all the models and some exceptions remain.

Examination of the 22 regional flux estimates across the models further indicates some relationships to the background flux responses, though generalization is much more challenging. For example, models with a strong response to the background ocean flux estimate the least uptake in both the Southern Ocean and northern ocean regions. Models with large west to east RCR gradients across North America and Europe are among the models with the greatest uptake in these regions. However, models with small gradients are not necessarily those with little uptake in these regions.

Table 5. *Posterior flux differences in Gt C yr^{-1} for inversion performed without background biosphere flux (control case minus 'No Rect' sensitivity test)*

Region\Model	CSU	UCB	UCI	UCIs	UCIb	JMA	MATCH: CCM3	MATCH: NCEP	MATCH: MACCM2	NIES	NIRE	RPN	SKYHI	TM2	TM3	GCTM	CSIRO
Boreal NA	0.48	−0.32	−0.39	−0.41	−0.31	−0.12	−0.05	−0.14	−0.29	0.03	−0.26	−0.04	0.07	0.05	0.09	0.25	0.11
Temperate NA	−0.30	0.89	1.01	0.88	1.04	0.33	0.38	0.28	0.88	−0.01	−0.16	−0.40	−0.06	0.28	0.25	0.35	0.26
Tropical America	0.32	−0.08	−0.42	−0.80	−0.59	−0.11	−0.03	0.09	0.31	0.23	−0.17	−0.07	−0.55	−0.34	−0.06	−0.38	−0.26
South America	0.02	0.29	0.14	0.27	0.16	0.06	−0.03	−0.25	−0.07	0.22	−0.25	−0.10	0.08	0.01	−0.20	−0.02	−0.33
Northern Africa	0.68	0.80	−0.25	−0.66	−0.03	0.54	−0.12	1.52	0.67	1.41	1.09	0.12	1.48	0.30	0.75	1.05	1.02
Southern Africa	0.10	−0.58	0.41	0.49	0.41	0.17	0.05	−0.79	−0.04	−0.23	0.36	0.56	0.37	−0.28	−0.22	−0.07	0.01
Boreal Asia	−0.90	−1.15	−0.29	−0.83	−0.48	−1.57	−1.45	−1.76	−2.02	−1.69	−1.35	−0.36	−0.83	−0.73	−1.39	−1.24	−1.89
Temperate Asia	0.03	−0.09	−0.37	0.67	−0.34	0.44	0.58	0.66	−0.29	0.59	1.20	1.63	0.04	0.74	0.00	1.01	0.90
Tropical Asia	0.11	0.58	−0.12	−0.31	−0.01	−0.19	0.30	0.64	0.26	−0.20	−0.06	−0.21	−0.06	−0.15	0.17	−0.12	0.07
Australia	−0.05	0.03	0.00	0.01	0.01	0.07	0.04	0.19	0.06	0.01	−0.05	−0.01	0.00	0.00	0.07	0.14	0.13
Europe	0.33	−0.37	0.21	0.16	0.14	0.36	−0.02	−0.35	0.53	−0.02	0.46	−0.18	0.25	0.52	0.08	0.43	0.06
N Pacific	0.07	0.34	−0.03	0.35	−0.01	0.47	0.54	0.32	0.47	0.34	−0.41	−0.13	−0.41	−0.44	0.36	−0.40	0.32
W Pacific	−0.32	−0.18	−0.30	0.12	−0.26	−0.30	−0.19	−0.23	−0.16	−0.56	−0.42	−0.23	−0.35	−0.16	−0.18	−0.16	−0.41
E Pacific	0.21	0.24	0.31	0.02	0.33	−0.17	0.12	−0.26	−0.03	0.16	0.11	−0.03	−0.01	0.03	−0.03	0.12	0.05
S Pacific	−0.06	0.15	0.35	0.42	0.33	0.07	0.24	0.07	0.06	0.26	0.43	0.33	0.18	0.31	0.37	0.15	−0.04
Northern Ocean	−0.10	−0.03	−0.10	−0.07	−0.08	0.05	0.03	0.13	−0.03	0.06	−0.05	0.07	−0.12	0.01	0.04	−0.37	0.03
N Atlantic	−0.49	−0.24	−0.14	−0.26	−0.23	0.07	−0.38	−0.05	−0.22	−0.08	−0.40	−0.38	0.01	−0.09	0.17	−0.27	−0.18
Tropical Atlantic	−0.26	−0.17	−0.13	0.02	−0.12	−0.01	−0.07	−0.11	−0.03	0.01	0.17	−0.06	0.14	−0.01	−0.09	−0.12	0.20
S Atlantic	−0.05	−0.09	−0.01	0.05	−0.01	−0.01	−0.02	−0.12	−0.13	−0.17	0.00	−0.04	−0.15	−0.07	−0.14	−0.23	0.02
Southern Ocean	−0.10	−0.13	−0.22	−0.16	−0.21	−0.09	−0.11	−0.02	−0.04	−0.11	−0.01	−0.15	−0.05	−0.02	−0.11	−0.08	−0.09
Trop Indian Ocean	0.33	0.17	0.34	0.13	0.29	−0.05	0.20	0.11	0.08	−0.24	−0.13	−0.37	−0.08	0.01	0.08	−0.11	−0.07
S Indian Ocean	−0.06	−0.05	−0.02	−0.08	−0.05	−0.57	−0.01	0.07	0.04	0.00	−0.13	0.07	0.05	0.05	−0.02	0.06	0.06
Glbl offset (ppm)	0.02	−0.20	−0.21	−0.26	−0.22	−0.09	−0.80	−0.15	−0.14	−0.03	−0.10	−0.24	−0.14	−0.10	−0.09	−0.02	0.06

Furthermore, the estimated fluxes in northern extratropical Asia appear to have a limited relationship to the distribution of background flux response. Asia, however, is where the largest changes occur in individual model flux estimates when the background biosphere exchange is removed from the inversion. Most models exhibit large changes in their estimated flux when this change is made, often changing from a sink to a source.

In many instances, the model-to-model differences appear to reflect particular individual model responses at stations. Some of this is due to the coincidence of large concentration gradients and station locations, while some may be due to local transport differences at the surface, such as convective transport or the construction of the planetary boundary layer (PBL).

In contrast to the individual model flux estimates, the model mean fluxes outside of the tropical regions appear to be relatively insensitive to changes in estimates of the prior fluxes and prior flux uncertainties. Less uptake in the Southern Ocean than has been implied by oceanographic observations and a large and an evenly distributed sink over the northern continents remain despite dramatically increasing the uncertainty bounds on the prior fluxes, eliminating the prior fluxes, or eliminating the biospheric and oceanic background fluxes. In this sense the model mean estimates can be considered robust to these aspects of the inversion setup. A companion study (Law et al., 2003) finds the model mean flux estimates to be relatively insensitive to variations in the incorporation of the observational data.

A better understanding of regional carbon budgets in the middle latitudes depends on improving the simulated transport, whereas confidence in fluxes over the tropical continents is primarily limited by sparse data. The tropical land fluxes are determined primarily by global mass balance and the fluxes in better observed regions such as the northern extratropical regions. Combined with the lack of observational constraint is the tendency for deep mixing in the tropics, which leads to weak responses at the surface in these regions. The tradeoff between an uncertain rectifier in the northern extratropics and the poor tropical data constraint induces compensating fluxes. Models with strong rectifiers are able to generate large northern uptake and still maintain global mass balance by introducing large tropical sources, and vice versa. Improving the tropical observations might therefore provide a better constraint on the rectifier effect and therefore on mid-latitude fluxes. Conversely, a better understanding of northern rectifier effects would probably produce better estimates of tropical carbon budgets.

5. Acknowledgements

This work was made possible through support from the National Science Foundation (OCE-9900310), the National Oceanic and Atmospheric Administration (NA67RJ0152, Amend 30) and the International Geosphere Biosphere Program/Global Analysis, Interpretation and Modeling Project. S. Fan and J. Sarmiento acknowledge support from NOAA's Office of Global Programs for the Carbon Modeling Consortium.

REFERENCES

Andres, R. J., Marland, G., Fung, I. and Matthews, E. 1996. Distribution of carbon dioxide emissions from fossil fuel consumption and cement manufacture, 1950–1990. *Global Biogeochem. Cycles* **10**, 419–429.

Apps, M. J. and Kurz, W. A. 1994. The role of Canadian forests in the global carbon balance. In: *Carbon Balance on World's Forested Ecosystems: Towards a Global Assessment* (ed.M. Kanninen) Academy of Finland, Helsinki, 14–39.

Arakawa, A. and Schubert, W. H., 1974. Interaction of a cumulus cloud ensemble with the large-scale environment, Part I. *J. Atmos. Sci*. **31**, 674–701.

Baker, D. F. 2001. *Sources and Sinks of Atmospheric CO_2 Estimated from Batch Least-Squares Inversions of CO_2 Concentration Measurements*. Ph.D. Dissertation, Princeton University.

Benoit, B. M., Desgagné, M., Pellerin, P., Pellerin, S., Chartier, Y. and Desjardins S. 1997. The Canadian MC2: A semi-Lagrangian, semi-implicit wideband atmospheric model suited for finescale process studies and simulation. *Mon. Wea. Rev*. **125**, 2382–2415.

Bousquet, P., Ciais, P., Peylin, P., Ramonet, M. and Monfray, P. 1999a. Inverse modeling of annual atmospheric CO_2 sources and sinks 1. method and control inversion. *J. Geophys. Res*. **104**, 26161–26178.

Bousquet, P., Peylin, P., Ciais, P., Ramonet, M. and Monfray, P. 1999b. Inverse modeling of annual atmospheric CO_2 sources and sinks 2. sensitivity study. *J. Geophys. Res*. **104**, 26179–26193.

Bousquet, P., Peylin, P., Ciais, P., Le Quéré, C., Friedlingstein, P. and Tans, P. 2000. Regional changes in carbon dioxide fluxes of land and oceans since 1980. *Science*, **290**, 1342–1346.

Brenkert, A. L. 1998. Carbon dioxide emission estimates from fossil-fuel burning, hydraulic cement production,

and gas flaring for 1995 on a one degree grid cell basis. (http://cdiac.esd.ornl.gov/ndps/ndp058a.html).

Ciais, P., Tans, P., White, J. W. C., Trolier, M., Francey, R. and coauthors. 1995. Partitioning of ocean and land uptake of CO_2 as inferred by $\delta^{13}C$ measurements from the NOAA Climate Monitoring and Diagnostics Laboratory Global Air Sampling Network. *J. Geophys. Res*. **100**, 5051–5070.

D'Andrea, F. S., Tibaldi, S., Blackburn, M., Boer, G., Deque, M. and coauthors. 1998. Northern Hemisphere atmospheric blocking as simulated by 15 atmospheric general circulation models in the period 1979–1988. *Climate Dynam.* **14**, 385–407.

De Fries, R. S. and Townshend, J. R. G. 1994. NDVI-derived land cover classifications at a global scale. *Int. J. Remote Sens*. **15**, 3567–3586.

Denning, A. S., Fung, I. Y. and Randall, D. A. 1995. Latitudinal gradient of atmospheric CO_2 due to seasonal exchange with land biota. *Nature* **376**, 240–243.

Denning, A. S., Randall, D. A., Collatz, G. J. and Sellers, P. J. 1996. Simulations of terrestrial carbon metabolism and atmospheric CO_2 in a general circulation model. Part 2: Spatial and temporal variations of atmospheric CO_2. *Tellus* **48B**, 543–567.

Denning, A. S., Holzer, M., Gurney, K. R., Heimann, M., Law, R. M. and coauthors. 1999. Three-dimensional transport and concentration of SF_6: A model intercomparison study (TransCom 2). *Tellus* **51B**, 266–297.

Ding, P. and Randall, D. A. 1998. A cumulus parameterization with multiple cloud base levels. *J. Geophys. Res*. **103**, 11341–11354.

Dixon, R. K., Brown, S., Houghton, R. A., Solomon, A. M., Trexler, M. C. and Wisniewski, J. 1990. Carbon pools and flux of global forest ecosystems. *Science*, **263**, 185–190.

Engelen, R. J., Denning, A. S., Gurney, K. R. and TransCom 3 modelers. 2003. On error estimation in atmospheric CO_2 inversions. *J. Geophys. Res*. **107(02)**, 4635, doi:10.1029/2002JD002195.

Enting, I. 2002. *Inverse Problems in Atmospheric Constituent Transport*. Cambridge University Press, Cambridge, U. K.

Enting, I. G. and Mansbridge, J. V. 1989. Seasonal sources and sinks of atmospheric CO_2: Direct inversion of filtered data. *Tellus* **41B**, 111–126.

Enting, I. G., Trudinger, C. M. and Francey, R. J. 1995. A synthesis inversion of the concentration and $\delta^{13}C$ of atmospheric CO_2, *Tellus* **47B**, 35–52.

Fan, S., Gloor, M., Mahlman, J., Pacala, S., Sarmiento, J. and coauthors. 1998. A large terrestrial carbon sink in North America implied by atmospheric and oceanic CO_2 data and models. *Science* **282**, 442–446.

GLOBALVIEW-CO_2, Cooperative Atmospheric Data Integration Project - Carbon Dioxide, CD-ROM, NOAA CMDL, Boulder, Colorado, 2000.

Gurney, K., Law, R., Rayner, P. and Denning, A. S. 2000. TransCom 3 Experimental Protocol, Department of Atmospheric Science, Colorado State University, USA, Paper No. 707. http://transcom.colostate.edu/TransCom_3/transcom_3.html

Gurney, K. R., Law, R. M., Denning, A. S., Rayner, P. J., Baker, D. and coauthors. 2002. Towards robust regional estimates of CO_2 sources and sinks using atmospheric transport models. *Nature* **415**, 626–630.

Hack, J. J. 1993. Description of the NCAR community climate model (CCM2). NCAR/TN-382, 108 pp.

Hack, J. J. 1994. Parameterization of moist convection in the National Center for Atmospheric Research community climate model (CCM2). *J. Geophys. Res*. **99**, 5551–5568.

Hamilton, K., Wilson, R. J., Mahlman, J. D. and Umscheid, L. J. 1995. Climatology of the SKYHI troposphere–startosphere–mesosphere general circulation model. *J. Atmos. Sci*. **52**, 5–43.

Hansen, J., Sato, Mki., Ruedy, R., Lacis, A., Asamoah, K. and coauthors. 1997. Forcings and chaos in interannual to decadal climate change. *J. Geophys. Res*. **102**, 25679–25720.

Hartke, G. J. and Rind, D. 1997. Improved surface and boundary layer models for the Goddard Institute for Space Studies general circulation model. *J. Geophys. Res*. **102**, 16407–16422.

Heimann, M. 1995. The global atmospheric tracer model TM2, Technical Report, 10, Deutsches Klimarechenzentrum, Hamburg, Germany, 51 pp.

Holtslag, A. A. M. and Boville, B. A. 1993. Local versus nonlocal boundary-layer diffusion in a global climate model. *J. Climate* **6**, 1825–1842.

Houghton, R. A. 1999. The annual net flux of carbon to the atmosphere from changes in land use 1850–1990. *Tellus* **51B**, 298–313.

Houghton, R. A. and Hackler J. L. 1999. Emissions of carbon from forestry and land-use change in tropical Asia. *Global Change Biol*. **5**, 481–492.

Kaminski, T., Heimann, M. and Giering, R. 1999. A coarse grid three-dimensional global inverse model of the atmospheric transport, 2. Inversion of the transport of CO_2 in the 1980s. *J. Geophys. Res*. **104**, 18555–18581.

Kaminski, T., Rayner, P. J., Heimann, M. and Enting, I. G. 2001. On aggregation errors in atmospheric transport inversion. *J. Geophys. Res*. **106**, 4703–4715.

Kauppi, P. E., Mielikainen, K. and Kuusela, K. 1992. Biomass and carbon budget of European forests 1971–1990. *Science* **256**, 70–74.

Keeling, C. D., Piper, S. C. and Heimann, M. 1989. A three-dimensional model of atmospheric CO_2 transport based on observed winds: 4. Mean annual gradients and interannual variations. In: *Aspects of Climate Variability in the Pacific and the Western Americas, Geophysical Monograph 55*. (ed. D. H. Peterson), AGU, Washington, D.C., 305–363.

Koch, D. and Rind, D. 1998. 10Be/7Be as a tracer of stratospheric transport. *J. Geophys. Res*. **103**, 3907–3917.

Kurz, W. A. and Apps, M. J. 1999. A 70 year retrospective analysis of carbon fluxes in the Canadian forest sector. *Ecol. Appl.* **9**, 526–547.

Law, R. M., Rayner, P. J., Denning, A. S., Erickson, D., Heimann, M. and coauthors. 1996. Variations in modelled atmospheric transport of carbon dioxide and the consequences for CO_2 inversions. *Global Biogeochem. Cycles* **10**, 783–796.

Law, R. M. 1999. CO_2 sources from a mass-balance inversion: Sensitivity to the surface constraint. *Tellus* **51B**, 254–265.

Law, R. M. and Rayner, P. J. 1999. Impacts of seasonal covariance on CO_2 inversions. *Global Biogeochem. Cycles* **13**, 845–856.

Law, R. M., Chen, Y-H., Gurney, K. R., and TransCom 3 modelers. 2003. TransCom 3 CO_2 inversion intercomparison: 2. Sensitivity of annual mean results to data choices. *Tellus* **55B**, this issue.

Levy, H., Mahlman, J. D., and Moxim, W. J. 1982. Tropospheric N_2O Variability. *J. Geophys. Res*. **87**, C4, 3061–3080.

Louis, J. F. 1979. A parameteric model of vertical eddy fluxes in the atmosphere. *Boundary-Layer Meteord*. **17**, 187–202.

Mahlman, J. D. and Moxim, W. J. 1978. Tracer simulation using a global general circulation model: results from a midlatitude instantaneous source experiment. *J. Atmos. Sci*. **35**, 1340–1374.

Mahlman, J. D., Pinto, J. P. and Umscheid, L. J. 1994. Transport, radiative, and dynamical effects of the Antarctic ozone hole: A GFDL "SKYHI" model experiment. *J. Atmos. Sci*. **51**, 489–508.

Maksyutov, S. and Inoue, G. 2000. Vertical profiles of radon and CO_2 simulated by the global atmospheric transport model. In: CGER report, CGER-I039-2000, CGER, NIES, Japan, v.7, 39–41.

McGregor J. L. 1996. Semi-Lagrangian advection on conformal-cubic grids. *Mon. Wea. Rev*. **124**, 1311–1322.

McGregor J. L. and Dix, M. R. 2001, The CSIRO Conformal-Cubic Atmospheric GCM, *IUTAM Symposium on Advances in Mathematical Modeling of Atmosphere and Ocean Dynamics*. Kluwer Academic Publishers, Dordrecht, 197–202.

Pacala, S. W., Hurtt, G. C., Baker, D., Peylin, P., Houghton, R. A. and coauthors. 2001. Convergence of land- and atmosphere-based U. S. carbon sink estimates. *Science* **292**, 2316–2320.

Prather, M. 1986. Numerical advection by conservation of second-order moments. *J. Geophys. Res*. **91**, 6671–6681.

Prather, M., McElroy, M., Wofsy, S., Russell, G. and Rind, D. 1987. Chemistry of the global troposphere: fluorocarbons as tracers of air motion. *J. Geophys. Res*. **92**, 6579–6613.

Randall, D. A., Shao Q. and Moeng, C.-H. 1992. A second-order bulk boundary-layer model. *J. Atmos. Sci*. **49**, 1903–1923.

Randall, D. A. and Pan, D.-M. 1993. Implementation of the Arakawa-Schubert parameterization with a prognostic closure. In: *The Representation of Cumulus Convection in Numerical Models* (eds.K. Emanuel and D. Raymond). American Meteorological Society, Boston, MA, 137–144.

Randerson, J. T., Thompson, M. V., Conway, T. J., Fung, I. Y. and Field, C. B. 1997. The contribution of terrestrial sources and sinks to trends in the seasonal cycle of atmospheric carbon dioxide. *Global Biogeochem. Cycles* **11**, 535–560.

Rasch, P., Mahowald, N. M. and Eaton, B. E. 1997. Representations of transport, convection and the hydrologic cycle in chemical transport models: Implications for the modeling of short lived and soluble species. *J. Geophys. Res*. **102**, 28127–28138.

Rayner, P. J., Enting, I. G., Francey, R. J. and Langenfelds, R. L. 1999. Reconstructing the recent carbon cycle from atmospheric CO_2, $\delta^{13}C$ and O_2/N_2 observations. *Tellus* **51B**, 213–232.

Ritchie H. and Beaudoin, C. 1994. Approximations and sensitivity experiments with a baroclinic semi-Lagrangian spectral model. *Mon. Wea. Rev*. **122**, 2391–2399.

Russell, G. L. and Lerner, J. A. 1981. A new finite-differencing scheme for the tracer transport equation. *J. Appl. Meteorol*. **20**, 1483–1498.

Schimel, D. S., House, J. I., Hibbard, K. A., Bousquet, P., Ciais, P. and coauthors. 2001. Recent patterns and mechanisms of carbon exchange by terrestrial ecosystems. *Nature* **414**, 169–172.

Schubert, S., Rood, R. and Pfaendtner, J. 1993. An assimilated dataset for Earth science applications. *Bull. Am. Meteorol. Soc*. **74**, 2331–2342.

Sellers, P. J., Randall, D. A., Collatz, G. J., Berry, J. A., Field, C. B. and coauthors. 1996. A revised land surface parameterization (SiB2) for atmospheric GCMs. Part I: model formulation. *J. Climate* **9** 676–705.

Strahan, S. E. and Mahlman, J. D. 1994. Evaluation of the GFDL "SKYHI" general circulation model using aircraft N_2O measurements: 2. Tracer variability and diabatic meridional circulation. *J. Geophys. Res*. **99**, 10319–10332.

Suarez, M. J., Arakawa, A. and Randall, D. A. 1983. Parameterization of the planetary boundary layer in the UCLA general circulation model: Formulation and results. *Mon Wea. Rev*. **111**, 2224–2243.

Taguchi, S. 1996. A three-dimensional model of atmospheric CO_2 transport based on analyzed winds: Model description and simulation results for TRANSCOM. *J. Geophys. Res*. **101**, 15099–15109.

Takahashi, T., Wanninkhof, R. H., Feely, R. A., Weiss, R. F., Chipman D. W. and coauthors. 1999. Net sea–air CO_2 flux over the global oceans: An improved estimate based on the sea–air pCO_2 difference. Proceedings of the 2nd CO_2 in Oceans Symposium, Tsukuba, Japan.

Tans, P. P., Fung, I. Y. and Takahashi, T. 1990 Observational constraints on the global atmospheric CO_2 budget. *Science* **247**, 1431–1438.

Taylor, K. E., Williamson, D. and Zwiers, F. 1997. AMIP II Sea Surface Temperature and Sea Ice Concentration Boundary Conditions. (http://www-pcmdi.llnl.gov/amip/AMIP2EXPDSN/BCS/amip2bcs.html).

Tiedke, M. 1989. A comprehensive mass flux scheme for cumulus parameterization in large-scale models. *Mon. Wea. Rev*. **117**, 1779–1800.

UNFCCC. 2000. United Nations Framework Convention on Climate Change, National Communications from Parties Included in Annex 1 to the Convention: Greenhouse Gas Inventory Data from 1990 to 1998 (FCCC/SBI/2000/11).

Zhang, G. J. and McFarlane, N. A. 1995. Sensitivity of climate simulations to the parameterization of cumulus convection in the Canadian Climate Centre general circulation model. *Atmos. Ocean* **33**, 407–446.